

<sup>1</sup> Masters Thesis: The Evolution of Fault Slip  
<sup>2</sup> Surfaces with Cumulative Displacement

<sup>3</sup> Kelian Dascher-Cousineau

<sup>4</sup> May 15, 2017

<sup>5</sup> **Abstract**

<sup>6</sup> Fault slip surface roughness determines fault strength, friction and dy-  
<sup>7</sup> namic fault processes. Wear models and field observations suggest that  
<sup>8</sup> roughness decreases with cumulative displacement. However, measurements  
<sup>9</sup> have yet to isolate the effect of displacement from other possible controls,  
<sup>10</sup> such as lithology or tectonic setting. We present an unprecedentedly large  
<sup>11</sup> fault surface dataset collected in and around the San-Rafael Desert, S.E.  
<sup>12</sup> Utah, United States. In the study area, faults accommodated regional ex-  
<sup>13</sup> tension at shallow 1 to 3 *km* depth and are hosted in the massive, well  
<sup>14</sup> sorted, high porosity Navajo and Entrada sandstones. Existing detailed  
<sup>15</sup> stratigraphic throw profile provide a maximum constraint for displacement.  
<sup>16</sup> Where cross-sectional exposure is good, we measure exact displacement im-  
<sup>17</sup> parted on slip surfaces using offset in marker horizons. Thereby, we isolate  
<sup>18</sup> for the effect of displacement during the embryonic stages of faulting (0  
<sup>19</sup> to 60 *m* in displacement). Our field observations indicate a clear compo-  
<sup>20</sup> sitional and morphological progression from isolated joints or deformation

bands towards smooth, continuous and mirror-like fault slip surfaces with increasing displacement. To quantify these observations, slip surfaces were scanned with a white light interferometer, a laser scanner and a ground based Lidar. Together these instruments resolve more than eight decades of spatial bandwidth (from less than  $\mu m$ 's to  $m$ 's in scale). In so doing, to the best of our knowledge, we increase the existing data on published fault topographies by XXX fold (available HERE). Results indicate that roughness as defined by the power ( $P$ ) at a given wavelength ( $\lambda$ ) decreases with displacement ( $D$ ) according to a power law,  $P(\lambda) \propto D^{0.6 \pm 0.1}$ . Trends are however subject to significant scatter. Roughness measurement associated with only maximum constraints on displacements corroborate this result—for a given displacement, minimum roughness is bounded by the later smoothing trend. In addition, we find that the maximum roughness is fixed—bounded a by a primordial roughness corresponding to that of joints surfaces and deformation band edges. Building upon our results, we propose a wear model to explain the evolution of faults with displacement. The basis of the model is supported by numerical simulations of crack initiation and growth using boundary element models Fri2D and growth by work-minimization (GROW). Our modelling provides the first insight into fault slip surface process consistent with observational constraints, i.e. fractal geometry and a nearly power-law decay with displacement, by using calling upon scale dependent strength, strength heterogeneity and scale invariant asperity failure by truncation.

<sup>44</sup> **Contribution of Authors**

<sup>45</sup> **1 Introduction**

<sup>46</sup> **1.1 Context**

<sup>47</sup> Faults are a characteristic feature of the Earth’s brittle crust. Crustal permeability,  
<sup>48</sup> seismicity, and mineralization are just few systems upon which faults act as major  
<sup>49</sup> controls [96, 97]. In spite of their importance, some aspects of faults and their  
<sup>50</sup> underlying processes remain poorly understood. What are the frictional properties  
<sup>51</sup> of faults? How strong is a fault? How do faults mature as they evolve from  
<sup>52</sup> small to large displacement structures? Key factors such as pore pressure [?, 17],  
<sup>53</sup> mineral composition [?, 28, 99] and fault architecture [25, 26] have been shown  
<sup>54</sup> to have important roles in the behavior of faults. However, these factors often  
<sup>55</sup> fail to explain the highly heterogeneous, chaotic and hierarchical behaviour of  
<sup>56</sup> faults. Complex fault geometry has long been proposed as a key factor in the  
<sup>57</sup> faulting process. However, a detailed and robust exploration of the implications  
<sup>58</sup> thereof has only recently garnered increasing attention. This change of pace mainly  
<sup>59</sup> owes to advances in mathematical theory behind complex natural systems [59,  
<sup>60</sup> 60], rapid advances computational abilities enabling more complex source models,  
<sup>61</sup> technological advances in high resolution surveying tools (GPS, photogrammetry  
<sup>62</sup> and Lidar) and detailed field studies of fault architecture [22, 86]. Fault geometry  
<sup>63</sup> has since been included as a key component of wholistic explanations for the  
<sup>64</sup> mechanical behavior and evolution of faults (e.g. [1, 55, 86]).

<sup>65</sup> Fault zones generally comprise of a damage zone and fault core. The damage  
<sup>66</sup> zone represents the halo of subsidiary fault features including smaller fault, frac-

67 tures, cleavage and veins. The fault core generally represents the zone in which  
68 most of the displacement has taken place and is associated with intense comminu-  
69 tions of the protolith [18, 25, 96]. Actual Slip on a fault occurs on discrete slip  
70 surfaces within the fault core [?, 5, 39, 70]. These surfaces are not planar; they are  
71 rough [86]. Slickenlines, corrugations, mullions and jogs are all fault slip surface  
72 features which reflect the multiscale nature of fault roughness [78, 86]. Field stud-  
73 ies have found common characteristics in the statistical properties which describe  
74 the topography of fault surfaces. These can be summarized as follows: 1) Fault  
75 surfaces topographies appear to be well defined by large fractal domains [86] ,  
76 wherein 2) faults are smoother at larger length scales [?, 82] and 3) are rougher in  
77 the slip-perpendicular direction than in the slip-parallel direction [56, 82].

78 Fault roughness has been demonstrated to be critical in determining fault prop-  
79 erties and corresponding scaling relationships. A series of field investigations,  
80 laboratory experiments, analytical predictions and numerical simulation have ex-  
81 plored the heterogeneous stresses and deformation patterns around complex fault  
82 geometries around single fault steps, ramps and jogs (e.g. [7, 16, 51, 62, 89]), on  
83 simple theoretical fault geometries (e.g. [27, 29]), and real or synthetic faults with  
84 geometrically fractal bandwidths in two dimensions (e.g. [38, 46, 76, 80] and three  
85 dimensions (e.g. [63, 67, 91, 105, 106]). Direct repercussion of complex stress patterns  
86 include the following: increased geometrical shear resistance [41]; increased and  
87 spatially variable off-fault damage and fracture energy [27, 46, 68]; reduced stress  
88 drop [106] and impeded slip budget [37]. In numerical simulations, zielke2017fault  
89 reports a nearly two-fold decrease in earthquake moment release for a fault with  
90 realistic roughness compared to its planar counterpart. Laboratory experiments  
91 comparing smooth and rough surface show that with increasing roughness, friction

92 increases [8], slip stability decreases, critical slip distance increases and rupture  
93 nucleation dimension increases with surface roughness [?, 47]. These features do  
94 appear in earthquake statistics. Bolstered by numerical simulations of complex  
95 stress fields, Parsons, 2008, found that persistent clusters and gaps in seismicity  
96 can be attributed to geometrical complexities on faults.

97 It is increasingly evident that roughness is both a fingerprint of the fundamental  
98 features of- and an active agent in the faulting process [14, 21, 86]. In accordance,  
99 incorporating more complex sources geometries has become a more frequent prac-  
100 tice in dynamic earthquake rupture modelling and slip inversions (e.g. [65, 91, 106]).

101 The magnitude in roughness is highly variable. While there has been significant  
102 progress in understanding the active role of roughness in the faulting process, it  
103 remains unclear what determines the complexity of fault geometry (e.g. [14, 22]).  
104 Sagy et al. (2007) noted a systematic decrease in roughness of ‘mature’, large  
105 displacement faults compared to ‘immature’ faults with low displacements. Similar  
106 results have been observed along reactivated joints, in laboratory experiments [36],  
107 and in compilations of fault roughness analysis [13, 20]. However, these data show  
108 only weak correlations between fault roughness and cumulative displacement [13,  
109 22]. These results are also put in question by later experiments showing roughening  
110 with shear with normal loads higher than 7.5 MPa [6].

111 Relating fault roughness to cumulative displacement is not trivial. Experi-  
112 ments cannot perform tests with realistic roughness over large enough displace-  
113 ment. It is also unclear how laboratory experiments scale up to natural faults.  
114 Exhumed fault slip surfaces are rarely well preserved. Furthermore, obtaining  
115 well-constrained displacement estimates is contingent on the presence of precise  
116 and accurate kinematic indicators (e.g. piercing points). Additionally, combining

117 observations over a broad range of displacements is challenging. Consequently, it is  
118 unclear whether trends observed in compilations of roughness measurements from  
119 multiple faults are directly attributable to displacement or a combination other  
120 geological factors. For instance, while comparing fault surfaces from geologically  
121 diverse datasets, variations in lithology, faulting regimes, temperature and depth  
122 may all be introducing further systematic variations.

123 The existence of a distinction between mature and immature faults and the pre-  
124 cise characterization of this transition has far-reaching implications. As discussed  
125 above, earthquake sources parameters are sensitive to fault roughness. Corre-  
126 spondingly, an evolution of roughness with displacement implies that "not all  
127 fault should be treated equally". This prediction is consistent with more efficient  
128 energy radiation measured on mature faults compared to immature faults [48];  
129 and changes in b-values associated with fault off-set [98]. Additionally, the evolu-  
130 tion of roughness represents a novel insight into the architecture of a fault zone.  
131 The geometry of the fault surface modulates the architecture of the whole fault  
132 zone [46, 76]. Changes in roughness require interaction between the slip surfaces  
133 and its direct surrounding (fault core), resulting in the formation of fault rock [72]  
134 and off-fault damage [46, 76]. The co-evolution evolution of the fault slip sur-  
135 face and the fault zone as a whole is a novel insight the maturity of fault from a  
136 structural point of view.

## 137 1.2 Fault Roughness

138 The deviation of fault surfaces from planarity formally defines roughness [15]. Pi-  
139 oneering studies used contact profilometers to measure the roughness of fracture

<sup>140</sup> and fault surfaces along discrete profiles [15, 60, 71, 73, 86]. Combined with the sur-  
<sup>141</sup> face profile of the San Andreas fault, faults were found to exhibit fractal scaling  
<sup>142</sup> over a remarkably broad range of length scales ranging over 10 orders of magni-  
<sup>143</sup> tude—from  $10^{-5}$  to  $10^5 m$  [3, 73, 86]. Over these length scales, fractal scaling is said  
<sup>144</sup> to be statistically self-affine [59, 60].

<sup>145</sup> A statistically self-affine profile along  $x$  with heights  $h(x)$ , is invariant under  
<sup>146</sup> the affine transformation:

$$\begin{cases} x \rightarrow \lambda x \\ h \rightarrow \mu h \end{cases} \quad (1)$$

<sup>147</sup> This relation therefore implies an exponential relation between the scaling,  $\lambda$   
<sup>148</sup> (along  $x$ ), and  $\mu$  (along  $h$ ) such that:

$$\mu = \lambda^\varsigma \quad (2)$$

<sup>149</sup> Where  $\varsigma$  is a constant named the Hurst exponent [82].

<sup>150</sup> Many analytical methods exist to quantify the fractal roughness of faults [20,  
<sup>151</sup> 59, 84]. Possibly most intuitive of which is the Root Mean Squared (*RMS*) as a  
<sup>152</sup> function of scale. It is effectively a measure of topographic variance. For a given  
<sup>153</sup> profile of length  $L$  with a point spacing of  $\Delta x$  with deviation  $h$  from the best fit  
<sup>154</sup> line, the *RMS* is defined as follows:

$$RMS(L) = \sqrt{\frac{\Delta x}{L} \sum_{i=1}^{L/\Delta x} h_i^2} \quad (3)$$

<sup>155</sup> The *RMS* roughness of a fault or fracture exhibits power-law scaling with seg-  
<sup>156</sup> ment length. A self-affine profile should therefore plot as a straight line on a log-log

plot of the *RMS* as a function of the segment length with a slope equivalent to  
 the Hurst exponent [84]. The most conventional approach to describe the fractal  
 roughness of faults has instead been the power spectrum and variations thereof  
 (i.e. amplitude spectrum and power spectral density). By testing various frac-  
 tal analytical tools on synthetic profiles [84] and surfaces [20], the power spectral  
 analysis was shown to yield estimated of scaling exponent most robust to system  
 size and Hurst exponent values. For a set of discretely sampled points, the power  
 spectrum of a profile is the result of a Fourier transform. In practice it is obtained  
 using a Fast Fourier Transform algorithm (FFT). The power spectrum defines a  
 two dimensional surface profile as linear superposition of sinusoidal profiles dis-  
 cretized over a fixed frequency domain. In the frequency domain, rougher profiles  
 will have correspondingly higher amplitudes, or power. The power spectrum of a  
 self-affine profile defines a power-law:

$$P(k) = Ck^{(-1-2\zeta)} \quad (4)$$

Where  $P(k)$  is the power at a given spatial frequency,  $k$ ,  $C$  is the pre-factor and  
 $\zeta$  is the Hurst exponent [22, 59, 71, 82].

Pioneering studies suggested that fault surfaces were approximately self-similar.  
 Self-similarity represents a self-affinity with a Hurst exponent is 1 [59]. The devel-  
 opments in laser scanner technology over the past decade, particularly terrestrial  
 laser scanners, enabled the detailed characterization of slip surfaces in three di-  
 mension [9, 13, 22, 49, 52, 56, 75, 78, 79]. Later studies averaging result cross sectional  
 profiles through a fault surface suggested that smaller Hurst exponent may better  
 characterize fracture surfaces and faults (e.g. [21, 22, 56, 78, 82]). Studies of natural

mode I crack surfaces have observed radially sym self-affinity with a Hurst exponent of  $\sim 0.8$  at all scales of observation ([11, 83]-and references therein). Shear, or mode II cracks (i.e. faults) were found to differ in that they are anisotropic. The Hurst exponent parallel to shear ( $\sim 0.6$ ) is smaller than that in the shear-perpendicular direction ( $\sim 0.8$ ) [9, 22, 56, 79]. Overall, observations also show that fault surfaces have distinctly smoother profiles along slip direction than perpendicular to slip [?, 22, 56]. The magnitude of the roughness in both directions is, however, subject to a substantial spread in values over many orders of magnitude [13, 22]. This variability is most strongly reflected in the pre-factor. Recent studies also report a minimum length scale of grooving, a length scale at which slip surface is no longer anisotropic [14, 19]. This transitions typically occurs around 4 to  $500 \mu m$  and roughly corresponds to where the fractal scaling in the slip parallel and slip perpendicular direction meet.

Why are slip surfaces fractal? The fractal character of slip surfaces can be explained by a range of processes. There is, however, no clear consensus in the existing literature. Candidate explanations include the superposition of random wear processes processes, random fracture tip growth, and more ... Perhaps most topical is the proposition of scale dependent strength as proposed by Brodsky et al., 2016. Using the aspect ratios of geometrical asperities as a measure of rock strength at a given scale, it is argued that fractal character of fault surfaces directly reflects a scale dependence in rock strength. Moreover, a break in fractal scaling at the  $\approx XXX \mu m$  length scale is interpreted as a transitions from inelastic or brittle processes (large scales) to plastic processes. This explanations is in agreement with laboratory experiments that report that larger volumes of rock are, on average, weaker ...

204 Fractal characterizations of surfaces do not uniquely define a profile or surface.  
205 Other statistical metrics exist and are common place in many engineering practices.  
206 Specifically, examining the statistical distribution of the height measurements of  
207 a surface provides insight into the contact [?], frictional behavior [?] and wear  
208 processes [2].

209 define skewness, kurtosis, etc.

210 The the statistical moment is defined as follows:

211 First ( $m = 1$ ) and second ( $m = 2$ ) order

### 212 **1.3 The evolution of slip surfaces with displacement**

213 \*this could be in an interpretation section

214 Previous work has mainly associated fault surface deformation to mechanical  
215 wear processes as the dominant mechanism of surface evolution [13, 72, 79]. Me-  
216 chanical wear processes include any erosive process in which volume removal is  
217 frictionally induced from surfaces in sliding contact. Before further exploring the  
218 effects of wear in fault slip surfaces, it is worth recognizing that many other pro-  
219 cesses could—and likely do—cause the slip surface to evolve with displacement.

220 A surface can change according to the following:

221 *surface deformation*

222 *Addition of material*

223 *Removal of material*

224 Fault slip surfaces have evidence pointing to each of these processes preserved  
225 in the rock record.

226        *Surface deformation* encompasses any process by which a surface changes shape  
227        by the rearrangement of material (no removal or addition). Both elastic and  
228        inelastic processes allow fault blocks to deform. At the seismic time-scales, only  
229        elastic and brittle deformation can occur—whereby macroscopic fault damage and  
230        micro-fractures in grains and crystals away from the fault can enable stain and  
231        dissipate stress on the fault. At longer time-scales, calcite twinning, pressure  
232        solution, and clay alteration can also occur yield similar effects. These short and  
233        long-time scale mechanisms define the visco-elastic rheology of fault blocks.

234        It is unlikely that the rheology of the fault block and its effect on the slip  
235        surface topography are significant in the evolution of the slip surface. Using slick-  
236        enline orientations and fault core thickness as a proxy to the fault block rheology  
237        Kirkpatrick et al. 2014, find that 1) deformation does occurs in fault block and 2)  
238        there is a scale dependence to this deformation whereby. However, this scaling is  
239        not well represented in fault geometric scaling. It would rather predict a change in  
240        scaling at the outcrop scale. The absence of any such signal in the topography of  
241        fault slip surfaces implies that deformational processes cannot directly determine  
242        how slip surfaces evolve with displacement.

243        For its part, an *addition of material* occurs as fault rock is cemented onto slip  
244        surfaces—filling in geometrical concavities and effectively reducing the amplitude  
245        of surface irregularities. Its effect is preserved in the rock record with mobile, or  
246        *fluidized*, gouge cemented and re-fractured in subsequent faulting [78, 90]. More-  
247        over, it has been shown that discrete slip surface can arise from the localization of  
248        shear strain within unconsolidated granular material (e.g. [24]). It is key to note  
249        that this, and similar, mechanisms are then metered by the healing-rate and the  
250        wear-rate.

removal of material is caused by mechanical wear. As fault blocks slide past each other, frictional wear is an inevitable process. Layers of comminuted fault rock, cemented or not, are direct evidence of this process [72, 87]. Wear is known to be multiscale. At small scales, grains can be plucked or broken [90]; at larger scales grains plough slip surfaces to create corrugations [85] and sidewall ripouts form [100]. It is key to note that 1) all these processes fall under the definition of wear in that they involve the failure of geometrical protrusions, only these are expressed at various scales and 2) these have substantive impact on the surface geometry.

MAKE FIGURE HERE FOR REFERENCE SIMILAR TO THE ONE IN YOUR EPSL SLICKENLINE/RHEOLOGY PAPER - but focus on the fact that there is an asperity failing.

While wear processes are subject of a vast field of research, particularly in engineering and tribology due to interest in manufacturing machine parts for longevity [64], its applications in the earth sciences is emergent with tests mainly conducted at laboratory scales [?, 72, 87, 103]. The only applications to natural fault surfaces is a prediction of wear volume presented in Brodsky et al., 2011.

The wear rate, the volume of wear-product produced per unit offset is broadly related to the real area of contact and loading. When two surfaces are put in direct contact, the real area of contact is much smaller than the nominal surface areas because the load is supported at microscopic protrusions from a surface, or *asperities* ( [?, 2, 12, 45]). Remote loading normal to the surface causes local stresses and associated deformation at contact points. Note that as the load is increased, deformation of large asperities causes new asperities to come in contact. In its simplest form, wear rate ( $\frac{\partial V}{\partial x}$ ) is defined according to be proportional

276 to the remote load ( $P$ ):

$$\frac{\partial V}{\partial x} \propto P \quad (5)$$

277 The relation has been shown to be reasonably robust in experimentation for  
278 most materials. In further detail, the size, distribution and duration of contact  
279 areas, as well as the shape of the worn particles, control the general behaviour of  
280 wear. Note that material properties are contained in a constant of proportionality  
281 referred to as the probability factor—the probability of a collision of asperities to  
282 lead to removal of material [2].

283 Following this formulation, Scholz, 1987, proposed that wear rate for faults  
284 could be determined as a linear relationship with displacement and an inverse rela-  
285 tionship with hardness. The displacement relationship is in reasonable agreement  
286 with laboratory experiments [104] and measurements of natural fault rock thick-  
287 ness [77, 95]. The hardness dependence is difficult to test given uncertainties in  
288 both fault rock thickness and hardness [87]. The simple formulations forwarded  
289 by Archard, 1953, and its application to faults by Scholz, 1987, was acknowledged  
290 to have serious limitations in their applications to natural faults. Specifically, the  
291 author raises concerns about the surface geometry of real fault, and about the  
292 scaling and effectiveness of wear processes such as grains plucking and fault rock  
293 abrasion.

294 Building off of experiments on engineering metals [74] and ceramics [57], new  
295 fault wear model integrated a 'running-in' component which exponentially decays  
296 towards steady-state [72, 103]. This behavior introduced a discrete such that the  
297 volume of fault rock produced ( $V$ ) can be expressed as a function of displacement

298 ( $x$ ) according to:

$$V = \beta [1 - \exp(-nx)] + Kx \quad (6)$$

299 Where  $\beta$ ,  $n$ , and  $K$  are constants.

300 A running-in stage is thought to reflect effect of surface roughness. This later  
301 formulations was supported by a semi-analytical formulations of asperity failure  
302 and rotary shear experiments. However, in line with comments in Power et al.,  
303 1988, we propose that this running-in stage on real faults is likely to be substan-  
304 tially different for faults where fractal topography implies that new larger asperities  
305 will come into contact with increasing displacement. Laboratory experiments have  
306 limited fractal bandwidth. Shear boxes are limited to sample length; rotary shear  
307 apparatus are limited to their circumference length. We highlight that wear pro-  
308 cesses controlling the behaviour laboratory scale experiments are likely inadequate  
309 for natural faults. These may instead reflect relict behaviour issuing from limited  
310 fractal bandwidth and emplacement of mobile gouge layers buffering the surfaces.

311 It is clear that the fractal nature of fault surfaces is important to reconcile  
312 with a model of wear. Concepts of fractal scaling, strength heterogeneity and  
313 scale dependent strength are poorly captured by the current literature. Additional  
314 insight from field observations are needed to better understand fault slip surface  
315 processes. To date, notwithstanding preliminary efforts by Brodsky et al., 2011,  
316 linear scaling between fault rock thickness and displacement is nearly the only  
317 grounding field evidence for existing wear models (i.e. [72, 87, 103]). As pointed  
318 out by many authors [10, 40, 95] the scaling is contingent on highly uncertain  
319 and ambiguous measurements. Overlooking difficulties and/or inconsistencies in

320 determining displacement, the representative fault rock thickness is difficult to  
321 measure given variations of in thickness (often many orders of magnitude, even for  
322 a single outcrop), inconsistent definitions of the measurements across the literature,  
323 and potential breaks in scaling for certain faults.

324 The lack of a model grounded in more field observations, quantitative data and  
325 theoretically consistent with our current understanding of fault slip surfaces is a  
326 blaring knowledge gap that we seek to fill in this study.

## 327 **1.4 Faulting in Sandstone**

328 Faults in the well sorted Navajo and Entrada Sandstones in the San Rafael desert  
329 provide an ideal natural laboratory for the study of fault maturation. These have  
330 correspondingly been subject of extensive study of fault mechanics (e.g. [4, 5, 42,  
331 43, 54, 92–94] [44]). Its is however important to recognize faulting in sandstones  
332 such as the Navajo and Entrada units do have some peculuaritie that are worth  
333 outlining. Before presenting the tectonic and geological context of the the San  
334 Rafael desert, we first provide a brief overview of the existing litterature covering  
335 the nucleation, growth and coalescence of faults in sandstones with a specific focus  
336 on the areas presented in this study.

337 Two fault nucleation models exist faults in sandstone [4, 35], the first model  
338 is based on the localization of strain along deformation bands and deformation  
339 band clusters. Deformation bands are a characteristic feature of high porosity  
340 sediment [4, 5, 44]. Deformation bands define sinuous sheets which localise strain in  
341 zones typically less than a few millimetres in thickness [44]. Strain is accommodated  
342 by the run-away crushing of sedimentary grains and the concomitant collapse of

343 pore space. Strain across deformation bands is typically in shear [44]. Shear  
344 strain accommodated across a single deformation band is typically on the order of  
345 millimetres. With increasing shear strain, deformation bands coalesce in localized  
346 zones called deformation band clusters. It is characteristic for deformation bands,  
347 and deformation band clusters to protrude out of outcrop because of differential  
348 weathering. Field studies show that faults form in or along these deformation band  
349 clusters [4].

350 The second nucleation mechanism relies on the reactivation and coalescence  
351 of regional mesoscopic joint sets [35, 66]. Subsequent deformation leads to the  
352 formation of additional joints, sheared joints, zones of fragmentation, and, finally,  
353 through going slip surfaces enableb be the likage of splay fractures and joints  
354 (see figure [?]). This faulting mechanism is typically associated with more intense  
355 becciation and

356 The models have since been shown to be endmembers for the formation of faults  
357 in the High porosity sandstone such as that of the Navajo Desert presented in this  
358 study . Moreover, these mechanisms can act in unison and result in relatively  
359 complex overprinted architectures [35].

360 The maturation of faults in the Navajo and Entrada sandstones, and similar  
361 units in the region is particularly well recorded. In these units, the formation  
362 of pristine, slickensided slip surfaces is common and seemingly does not require  
363 large displacement form [4, 5]. While the evolution of slip surface with siplace-  
364 ment is not described in these field area (as will be done in this study), there has  
365 been substantial work describing the evolution and growth of damage zones with  
366 displacement which report roughly linear scaling laws over 0 to 50 meters of dis-  
367 placement [34, 92, 93]. Also, while it was typically though that defomation bands

368 pre-date the formation of faults [4,5], it was shown that later generations of defor-  
369 mation bands also form as a fault damage feature. The spatial density of deforma-  
370 tion bands and fault damage rapidly decreases with increasing distance from the  
371 fault according to a power law away from the center of the fault zone [92,93].The  
372 same field investigations reported no clear displacement scaling for fault core or  
373 fault rock over displacements ranging [92,95].

374 **1.5 Tectonic Setting**

375 The San Rafael Desert hosts a sequence of gently dipping marine and sub-areal  
376 sedimentary rocks deposited from the Pennsylvanian to the Jurassic (see Figure 2).  
377 The San Rafael Desert is part of the San Rafael Swell, a monocline that formed  
378 when these sediments were uplifted as a passive drape fold above a reactivated  
379 basement reverse fault during the Late Cretaceous Laramide Orogeny [50,102]. In  
380 turn, the swell is part of the broader Colorado Plateau [50]. Networks of joints and  
381 normal faults caused by Laramide activity cross-cut the sedimentary sequence and  
382 accommodate North-South extension [4,50]. Within the San Rafael Swell, we focus  
383 the following field locations: 1) the Chimney Rock Fault Array (Navajo Sandstone)  
384 [35,54,58], 2) the Big Hole fault (Navajo Sandstone) [92,93], 3) faults outcropped  
385 in the Iron Wash (Navajo Sandstone) [4,5] and 4) a network of deformation bands  
386 and faults near Goblin Valley State Park [4,5,42,43] (Entrada Sandstone) (see  
387 figure XXX). Table ?? present detailed descriptions of the Navajo and Entrada  
388 sandstone units.

389 Advantages of theses field locations are manifold. First, the nearly pure quartzite  
390 lithology, extensional tectonic regime, depth (2-4 km or 40-80 MPa), temperature

391 (estimates range from 45-90 °C) of activity, and faulting mechanism are all rela-  
392 tively consistent across all field areas [102]. Consistency in these parameters is key  
393 to isolating the effect of displacement on the fault roughness and is missing in any  
394 previous similar study of fault slip surfaces [13, 79]. Moreover, both field locations  
395 exhibit well preserved fault surfaces that are exposed and accessible (see Figure  
396 3).

397 The Chimney Rock fault array is an orthorhombic set of faults that crops out at  
398 the northern end of the San Rafael Swell ([35, 54]). Two sets of oppositely dipping  
399 normal faults crop out at the surface with preserved fault scarps. WNW-striking  
400 faults have clear evidence for fragmentation and are aligned with pre-existing joints  
401 and have correspondingly been interpreted to have formed by shear reactivation of  
402 joints, conversely ENE-striking faults have relatively more abundant deformation  
403 bands and show nearly no evidence of fragmentation and where therefore inter-  
404 preted to have formed from deformation bands (Davatzes, 2003). Exposure is very  
405 good, faults are abundant and have well preserved fault surfaces [102]. The Chim-  
406 ney Rock fault array has studied to better understand of fault geometry [92, 93],  
407 permeability [94] and kinematics [35, 54, 54, 58]. As a result, detailed maps of the  
408 fault array have been produced (e.g. [58]) . In addition, by using measurements of  
409 the separation between footwall and hanging wall cutoffs of sedimentary horizons,  
410 entire displacement profiles have been measured for faults with a wide range of  
411 displacements ([32, 58, 92, 93]). The Big Hole fault is located roughly 10 km to  
412 the South-East of the Chimney Rock Fault Array. While not explicitly part of  
413 the fault array, the Big Hole fault shares a nearly identical geological setting. The  
414 Big Hole fault has been extensively studied in detail as an analog to hydrocarbon  
415 reservoir-scale faults. Measurable displacements on the exposed fault range from

<sup>416</sup> 8 m to 39 m [92,93].

<sup>417</sup> Contrary to other field areas, Iron Wash, in the Navajo sandstone has not  
<sup>418</sup> featured a series of studies. However, it was mapped in detail by Aydin, 1977.  
<sup>419</sup> The area host a variety of normal, oblique and transform fault. Faults exposed  
<sup>420</sup> at Iron Wash are part of the Hawk's Nest fault system. The system has been  
<sup>421</sup> proposed to be related to the San Rafael Swell uplift [50]. Mapped displacement  
<sup>422</sup> range up to 80 m of offset. There are no large meters-scale slickensided surfaces.  
<sup>423</sup> However, it is possible to uncover small pristine slip surface sample on freshly  
<sup>424</sup> parted surfaces using a hammer and chisel. Here, displacement measurement are  
<sup>425</sup> readily obtainable by using the upper horizon of the Navajo sandstone, easily  
<sup>426</sup> distinguishable due to an disconformable contact also marked by a change in rock  
<sup>427</sup> color.

<sup>428</sup> Large networks of deformation band faults outcrop near Goblin Valley State  
<sup>429</sup> Park on the southeastern margin of the San-Rafael Swell ([5]. This locality com-  
<sup>430</sup> prises areas mapped in detail known as Molly's Castle and Horse Creek [4]. Because  
<sup>431</sup> deformation bands dramatically alter the local permeability structure, Goblin Val-  
<sup>432</sup> ley has been extensively studied in light of fault nucleation and the implications for  
<sup>433</sup> hydrocarbon circulation (e.g. [43, 101]). At Goblin valley, deformation band clus-  
<sup>434</sup> ters outcrop in iconic centimeter- to meter-sized slabs. These are often bounded  
<sup>435</sup> by discrete slip surfaces [5]. Offsets in sedimentary beds have allowed previous  
<sup>436</sup> studies to obtain detailed displacement measurements (e.g. [88]).

<sup>437</sup> Together, these field locations offer the chance to survey well-preserved fault  
<sup>438</sup> surfaces that have hosted displacements from embryonic stages to 55 m of displace-  
<sup>439</sup> ment. Moreover, novel to this study, we are able to survey multiple expressions  
<sup>440</sup> of a single fault's surface with various displacements according the displacement

<sup>441</sup> profile of the fault.

Table 1: Description of lithologies featured in this study [4]

	<b>Navajo</b>	<b>Carmel</b>	<b>Entrada</b>
<i>Age</i>	<i>Lower Jurassic</i>	<i>Middle Jurassic</i>	<i>Late Jurassic</i>
<i>Origin</i>	<i>Wind blown</i>	<i>Marine</i>	<i>Wind blown</i>
<i>Thickness</i>	$\sim 150\text{ m}$	$\sim 50\text{ m}$	$>150\text{ m}$
<i>Rock types</i>	<i>Sandstone, limey sandstone</i>	<i>Limestone, sandstone, siltstone, shale and Gypsum</i>	<i>Cross bedded sandstone, siltstone and shale</i>
<i>Composition</i>	$\sim 90\%$ quartz, 10% feldspar grains trace <1% ferromagnesia minerals calcite and silica cement		Quartz, feldspar and ferromagnesian minerals clay, calcite and quartz cement
<i>Mean Grain Size</i>	$\sim 0.05\text{ mm}$		$\sim 0.1\text{ mm}$
<i>Outcrop</i>	<i>Chimney Rock Big Hole Iron Wash</i>	<i>Chimney Rock</i>	<i>Iron Wash Molly's Castle</i>



Loca- tion	Lithology	Description	Displacement Constraints
Chim- ney Rock Fault Array	At the contact between the Navajo Sandstone and the base of the Carmel Unit	Orthorombic set of normal faults with preserved faults scarps of Navajo Sandstone	Displacement profiled of stratigraphic throw constrained by offset on a Carmel Limestone Marker Horizon by Maerten et al., 2000.
Big Hole Fault	Navajo Sandstone	One single large normal fault structure partitioning displacement on two major strands traceable for kilometers through a river wash with scarp exposure, and strike parallel/perpendicular cross-sectional exposure	Displacement constrained using the top Erosionally competent horizon at the top of the Navajo by Shipton and Cowie, 2003 and directly where possible.
Iron Wash	Navajo Sandstone	Network of normal and strike-slip cross-cutting faults. Little scarp exposure but has good cross-sectional exposure with fresh slip surfaces (using hammer and chisle)	Displacement mostly constrained by direct measurement of offset in the Upper Navajo horizon.
Molly's Castle	Entrada Sandstone	East-West striking network of normal faults and ubiquitous deformation bands. Well preserved slip surfaces broadly	Displacement constraints available in places from mapping by Aydin (1978) and directly measured using various marker

Table 2: Table caption

## <sup>444</sup> 2 Objectives

<sup>445</sup> This study fills a fundamental knowledge gap in the field of structural geology  
<sup>446</sup> and earthquake mechanics. While it is increasing evident that fault roughness  
<sup>447</sup> is an important agent in the earthquake process, it is still unclear what defines  
<sup>448</sup> the magnitude and large spread in roughness of fault slip surfaces. To do so, we  
<sup>449</sup> test the two following hypotheses: 1) fault slip surface geometry is defined by its  
<sup>450</sup> displacement history wherein 2) wear is the dominant mechanism of slip surface  
<sup>451</sup> evolution.

<sup>452</sup> These hypotheses are tested with three lines of inquiry:

- <sup>453</sup> 1. investigation of fault architecture and microstructure of faults in the San  
<sup>454</sup> Rafael Desert, Utah (section ??). Observations have a specific focus on  
<sup>455</sup> recording qualitative changes from zero displacements structures such as de-  
<sup>456</sup> formations bands and joints, to small displacement faults (centimeters of  
<sup>457</sup> displacements) and finally to larger faults (meters of displacement). We also  
<sup>458</sup> pay careful attention to the mechanisms that alter the slip surface geometry.
- <sup>459</sup> 2. geometric analysis of pristine fault surfaces preserved in the San Rafael  
<sup>460</sup> Desert , Utah, using scan data aquired in the field using a Lidar and a  
<sup>461</sup> laser scanner, and in the laboratory using white light interferometry (section  
<sup>462</sup> ??).
- <sup>463</sup> 3. numerical modelling failure of asperities using Boundary Element Modelling  
<sup>464</sup> (BEM) applied to frictional faults in two dimension (Fric2D - [30,31,33,81])  
<sup>465</sup> and crack growth by work-minimizations (GROW - [61]) (section ??).

<sup>466</sup> Building upon the results from each component, we propose a wear model for

<sup>467</sup> fault surfaces. This model calls upon scale dependent strength, strength hetero-  
<sup>468</sup> geneity and scale invariant asperity failure processes (section ??). Note that links  
<sup>469</sup> the scans of fault slip surfaces, Matlab scripts to process and analyse slip surfaces  
<sup>470</sup> and detailed documentation is available in the appendix.

## <sup>471</sup> **3 Field observations and Microstructure**

<sup>472</sup> We first report on the architecture of faults cutting the Navajo and Entrada Sand-  
<sup>473</sup> stones with a specific focus on the evolution from zero-displacement structures  
<sup>474</sup> such as joints and deformation bands to large offset structures with polished slip  
<sup>475</sup> surfaces and accompanying fault rock lithologies.

### <sup>476</sup> **3.1 Zero-Displacement Structures**

<sup>477</sup> The characteristics and surface morphology of the local zero-displacement fea-  
<sup>478</sup> tures are especially relevant to our analysis as they represent the initial, zero  
<sup>479</sup> displacement, roughness of faults in the study area. This is fundamental to  
<sup>480</sup> understanding the integrated maturation path of slip surfaces to larger displace-  
<sup>481</sup> ments [72].

#### <sup>482</sup> **3.1.1 Deformation Bands and Deformation Band Clusters**

<sup>483</sup> In outcrop exposure deformation bands are sinuous white lineaments. The sin-  
<sup>484</sup> uosity and the variability thereof both are notably higher than that of faults.  
<sup>485</sup> Accordingly, the trace of single deformation bands can be nearly as linear as small  
<sup>486</sup> faults; but can also form very arcuate paths. We note that isolated deformation  
<sup>487</sup> bands, far from faults, are typically less sinuous than those near faults and zones

488 of densely packed deformation bands. We observe a range in thickness for defor-  
489 mation bands of 1 to 5 millimeters in thickness. Maximum observed shear offset  
490 across a single deformation band is 10 cm but is more typically on the order of a  
491 few milimeters. Corresponding maximum shear strain is on the order of 10, but  
492 typically is on the order of unity as reported in fossen, 2007

493 Deformation bands often protrude out of outcrop as thin sheets (see figure  
494 2). The edges of the sheet are coated with single layer protolithic grain. A faint  
495 anisotropy, whereby the dip-direction (parallel to strain) is smoother than the hori-  
496 zontal direction (perpendicular to strain), is perceivable on the edges of protruding  
497 deformation band sheets.

498 In thin-section, bands are associated with a gradational reduction in grains  
499 size and an increase in angularity compared to the protolith (see figure 1). Along  
500 with the reduction of grain size, intra-granular fracture are much higher, grains  
501 are better packed and less porous.

502 Deformation band clusters contain groups, or clusters, of nearly co-planar, mu-  
503 tually cross-cutting individual bands. The clusters are dense networks of anasta-  
504 mozing deformation bands. The clusters range in thickness from a few millimetres  
505 to tens of centimetres in width, often outcropping as slabs up to meters in height.  
506 Clusters commonly form in upright conjugate pairs.

507 Deformation bands clusters have well defined edges. Given differential weath-  
508 ering, particularly characteristic for the Goblin Valley area, deformation bands  
509 form large meter-scale slabs. The exposed edges of deformation band clusters  
510 have distinctly corrugated and "lumpy" morphology (see figure 4-left). The cor-  
511 rugation is better defined than in individual deformation bands. The dip parallel  
512 rake of the corrugations is in general agreement with the normal, dip-slip, local

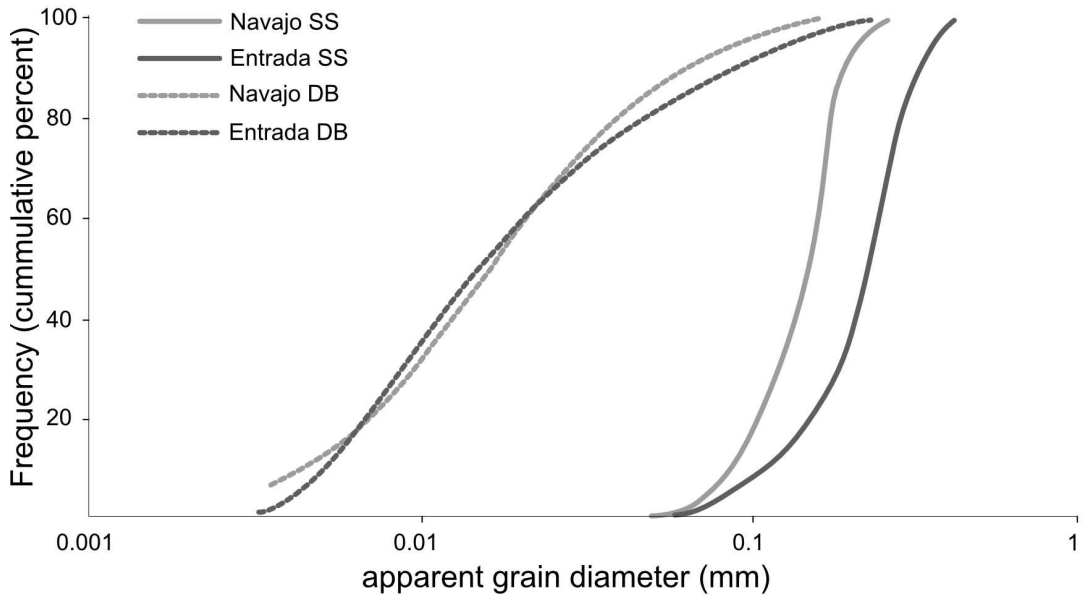


Figure 1: Grains size reduction of crushed grains within deformation bands relative to the undeformed sandstone units, the Navajo and Entrada sandstones. (figure adapted from Aydin, 1978)

513 kinematics. As is the case for individual deformation bands, edges of the defor-  
 514 mation band clusters are always coated with a cohesive, single grain-thick layer of  
 515 sand grains from the host sandstone. There is a clear directional asymmetry along  
 516 the direction of shear whereby steep faces are in the direction of shear offset and  
 517 shallowed faces are in the opposite directions (see figure 4). The asymmetry on  
 518 the hanging-wall edges of the slabs is inverted on the foot-wall edges likely indi-  
 519 cating an association with the overall kinematics of the clusters. Texture related  
 520 to deformation band clusters are poorly captured in thin section because the size  
 521 of any structural components exceeds the practical size of sections.



Figure 2: Example of single deformation bands protruding out of outcrop. A small deformation band cluster is also visible in the background.

522    **3.1.2 Joints**

523 Subvertical joints sets are a common feature of every locality. Joint sets are best  
 524 defined in the upper Navajo units and lower Carmel limestone pavements. The  
 525 abundance of joints increases near faults. Joints surface can be very large- effec-  
 526 tively defining cliff faces 10's or even 100's of meters in size. Joints are better  
 527 defined in the Navajo and Carmel Unit than in the Entrada. While spacing be-  
 528 tween joint in the Carmel pavements is tight (on the order of 10 cm), the spacing  
 529 in the Navajo appears to be much larger ( 1 m or more). Joint surfaces are notably  
 530 smoother than deformation bands, but rougher than slip surfaces. Salient mor-

531 phological features on joint surfaces are the plumose structures relict from fracture  
532 growth and fabrics aligned with cross-bedding horizons.



Figure 3: Left: Example of the edge of a deformation bands cluster at Molly's Castle. Note the "lumpy" morphology and an clear vertical directional asymmetry. Right: Cross-sectional view of a deformation band cluster with tens of centimeters of shear offset. It is unclear whether there is a through going slip surface localizing displacement. It is, however, definitely not on the edge of the cluster.

### 533 3.2 Slip Surfaces

534 Slip surfaces in the Navajo and Entrada sandstones are most readily identifiable  
535 by their relatively planar and polished morphology with a reflective or even vitre-  
536 ous polish. Striations and grooves on the slip surfaces mark the direction of slip.  
537 In cross-sectional exposure, slip surfaces are discrete, through-going and smooth  
538 relative to their zero-displacement counterparts. A sharp interface, separated by a  
539 sub-mm thick layer of incohesive white powder bounded by two vitreous surfaces.  
540 Thin milky white layers, less than a few centimetres in thickness, typically flank  
541 slip surfaces. These are in turn, within dense network deformation bands. The slip  
542 surfaces often cross-cut or bound deformation band clusters and the deformation  
543 bands within them. Perpendicular profiles are notably more sinuous than slip par-  
544 allel profiles. Slip surfaces are incohesive, and readily form a parting surface.(see

545 figure – figure similar to that in Jamies notes)

546 Slip surfaces are only preserved in the Navajo and Entrada Sandstones. For  
547 example, in spite of good exposures in prospecting pits and careful inspection of  
548 the slip zone, Navajo-Carmel contact at the Chimney Rock fault array does have  
549 preserved slip surfaces in the Carmel Unit. It is unclear whether this indicates that  
550 the Carmel units is more susceptible to erosion and/or alteration; or if a polished  
551 finish is only a feature of the quartzite sandstones.

552 Thin section observations reveal a layered micro-structural architecture of the  
553 faults rock locally bounding slip surfaces. The following succession, ordered ac-  
554 cording to distance from the slip surface is typical for slip surfaces in sand stone: 1)  
555 a very fine grained ultracataclastic layer, 2) a broader cataclasite layer (sometimes  
556 absent) and 3) a deformation band zone, the density of which gradually decreases  
557 into 4) the relatively intact protolith with disparate deformation bands.

558 The ultacataclasite is continuous, nearly always bounds the slip surface, and  
559 ranges from sub-milimeter to 2 milimeters in thickness. Texturally, the layer tex-  
560 turally overprints and cross-cuts all other layers. From visual assessment, the  
561 grain size distribution has a steep but continuous (no clast/matrix distinction) fall  
562 off with most grains being unresolvable at 400 fold magnification. Larger grains  
563 do not exceed 10's of micron - significantly smaller than protolithic intact grains  
564 which are on the order of 100's of micron. Grains have a large diversity in angu-  
565 larity ranging from sub-rounded to angular. We were unable to find fragmented  
566 counterpart within the ultracataclasite. This is indicative that the layer was likely  
567 fluidized [69]. There are partially offset survivor grains which could be interpreted  
568 as fragmented counterparts, however, these results from shear offset of fractures  
569 through-going the entire unlacataclastic layer. These fractures and grains they

570 partially offset are instead indicative of cycling between healing and brittle failure  
571 postdating the formation of the fluidized ultracataclastic layer. Ultracataclasite  
572 layers preserve a faint, potentially compositional, foliation oblique to the fault.  
573 Interpreted as S-type foliations, the kinematics from the flow banding are consis-  
574 tent with sense of shear of grains protruding into the ultracataclasite and partially  
575 sheared off. Previous work has shown no notable change in relative abundance of  
576 major elements, silicon, calcium, potassium and sodium, of the undeformed sand-  
577 stones [4]. We do however observe an increase in concentration in opaque oxides  
578 near the slip surface.

579 Scattered Electron Microscopy (SEM) reveals

580 A sharp, irregular and discontinuous interface juxtaposes the cataclastic layer  
581 to the ultracataclasite. The interface is characterized by a distinct difference in  
582 grain size and spatial arrangement. Past this transition, grains are larger and  
583 sometimes preserve damaged but intact sedimentary textures from the sandstone.

584 The interface between the ultracataclasite and the cataclasite is more irregular  
585 than the slip surface. The irregularity is broadly associated with the following  
586 two distinct length scales: the grain scale and the 'scalloping' length scale (see  
587 figure 5. Grains at the interface are typically truncated such that their tops are  
588 completely flattened. The transition towards flattened grains is well captured at  
589 various different stages by instances where grains protruding into the ultracata-  
590 clasite are still intact. ordered from least damaged to most damaged, we see the  
591 following: 1) grains that protrude into the ultracatclasite with little to no damage  
592 Other grains we evidence of healed internal cracks, 2) grains with various stages  
593 of micro-cracking and fractures, with fracture orientations roughly parallel to the  
594 slip and with some very small shear offset and, sometimes, rotation and 3) fully

595 cracked grain with the fragmented counterpart rotated along slip or completely  
596 missing missing. While most of the fractures are only intra-granular, some frac-  
597 tures can readily be projected into neighbouring grain.

598 A larger millimeter scale geometry can be traced from linking fractures. Both  
599 ends of the fractures abut in the ultracataclastic layer with shallow obliquity ( $15^\circ$ ),  
600 such that the crack follows an arcuate path with an overall 'scalloped geometry'.  
601 The occurrence of these fractures seem to be anticorellated with the thickness of  
602 the ultracataclasite. Again, this geometry is recorded at various stages ranging  
603 from the alignements of multiple fractures within the catacla

604 In contrast to the ultracataclasite, the original grain geometry is sometimes still  
605 discernible in the cataclasite. Grains size within the cataclasite layer is spatially  
606 variable with bands or lens' of larger grains separated by finer, more angular grains.  
607 These layers are texturally similar in overall geometry to deformation bands have  
608 much smaller grains.

609 This cataclastic layer thickness is highly variable. It typically ranges from  
610 millimetres to centimetres. Variability is directly associated with splay features  
611 which intensify mechanical damage around the fault. Its thickness on either side of  
612 the slip surface is often highly asymmetric. The layer is not always present. When  
613 it is absent, the fault, still bounded by a thin ultracataclasite, directly transitions  
614 into the intact host.

615 For certain faults, dark oxide filled fractures up to a few centimetres in length  
616 abut steeply into the slip surface and over-print other fault-related textural fea-  
617 tures. These are characteristically consistent with dynamics tensile cracks. If this  
618 interpretation is correct, they would indicative of seismic rupture velocities.

619 The evolution of slip surfaces with displacement is qualitatively apparent.

620 Faults with small displacements (centimetres of offset) are distinctly different than  
621 larger displacement faults (meters of offset). They are 1) visibly more sinuous, 2)  
622 laterally discontinuous, 3) less polished, instead, having a dull lustre, and 4) not  
623 bounded by well-defined gouge or cataclasites layers bounding the slip surface  
624 visible in the field. The minimum observed offset across slip surfaces was approx-  
625 imately 0.5 cm. It is unclear whether this lower bound is a mechanical transition  
626 between deformation with deformation bands and slip on a discrete slip surface.

627 Our observations suggest that a single surface does not always accommodate  
628 the bulk of the fault offset. Instead, fault zones often have many slip surfaces,  
629 sheared joints and splays which partition offset.

630 Certain slip surfaces do accommodate the overwhelming majority of fault offset–  
631 displacement accommodated by smaller neighbouring discontinuous slip surfaces  
632 is minimal (Shipton, XXX). Based on observations from previous workers and  
633 those made in this study where larger displacement slip surfaces are unambigu-  
634 ously identifiable, we generalized the characteristics of large offset slip surfaces for  
635 the Navajo and Entrada Sanstones as follows:

- 636 • *Large displacement slip surfaces are more discrete and planar.*
- 637 • *Larger displacement slip surfaces are not cross-cut by deformation bands or*  
638 *more sinuous and discontinuous slip surfaces*
- 639 • *large displacement slip surfaces are nearly cohesionless and forming easy*  
640 *parting surfaces*
- 641 • *Large displacement faults have a very vitreous finish;*
- 642 • *Large displacement slip surfaces are typically in the center of a damage zone.*

643       **Damage is an inevitable consequence of displacement and the ac-**  
644       **companying mismatch that accumulates. Damage at the field locations**  
645       **in this study is expressed as comminution (e.g. cataclasite and gouge),**  
646       **fragmentation (e.g. breccia, splay joints) and shear deformation (specif-**  
647       **ically deformation bands).**

648       In this study, we refer to *fault rock* as rocks associated with a fault (Snoke et  
649       al. 1998). The faults in our study area display a very diverse range in fault rock  
650       lithologies, ranging from fine-grained cataclasites to massive bodies of breccias (up  
651       to meters of thickness).

652       Fault rock consistently bounds slip surfaces—often asymmetrically. However,  
653       observations at the outcrop scale (10's of meters) both along the strike and dip  
654       indicate that both the lithology and thickness of the fault rock are highly heteroge-  
655       neous and are subject to large variability. These observations are consistent with  
656       more detailed fault architecture mapping conducted by Shipton et el., 2002.

657       We do not observe a clear and tractable relation between fault slip surface  
658       displacement and faults rock thickness. This is big part a result of difficulties in  
659       defining a clear fault rock thickness criterion which well encapsulates the variety  
660       of faults rocks – a challenge well highlighted in (Shipton et al., 2006).

661       \* this stuff is left over's from editing and moving things around

662       Healed Gouges

663       - the spot at big hole

664       - iron wash (powder between the surface)

665       - micro-structure

666       - prospecting pit

667       - typically on thinned sections of the fault rock (near the slip surface) Catacl-

668 asites . . .

669 - big hole sample with slip surfaces on both sides of the cataclasite

670 - micro-structure - Breccias . . .

671 - thick sections of the Breccias occur lenses which range from cm's to meters in

672 thickness. Breccia clasts are typically poorly sorted and can be very coarse with

673 clast up to 10 cm in diameter. Clasts show indications for multiple generations

674 of brecciation.

675 Thin Quarts lens - iron wash

676 Systematic associations between fault rock and fault structure exist. For in-

677 stance, Davatzes et al., 2002 reports of a systematic association between the fault

678 rock lithology and the orientation of the fault set. Namely, the orthorhombic fault

679 set striking WNW has systematic association with fragmentation—fault breccias;

680 conversely the ENE fault set rather has slip surfaces cutting through deformation

681 band clusters (see figure ??). This relation was speculated to be the result of

682 contrasting genetic mechanism. The WNW set is the result of the reactivation of

683 regional joints. In contrast the ENE fault set is the the result of clustering and

684 anastamosing deformation bands acting as a catalysing agent to the formation of

685 a faults. In this study, we observe clear instance of lithological contacts being

686 associated with brecciation (photo at iron wash where the top of the Navajo is

687 brecciated and quickly reverts to a single fault strand. More over, large breccia

688 bodies are clearly related to points where faults are cross-cutting each other at

689 high obliquity as is often the case at the Chimney Rock fault array and

690 Complicating factors:

691 Associations between brecciation and lithological contacts . . .

692 Associations between brecciation and cross cutting faults . . .

693 For an extensive review and description of the faults in the Navajo and Entrada  
694 sand stones refer to Aydin's thesis.

695 **3.3 Interpretation of field observations and roughness mea-  
696 surements**

697 Cross-cutting relationships reported bot in this study and in previous work on  
698 faults in the Navajo and Entrada units of the San-Rafael swell are particularly  
699 informative. Large displacement slip surfaces are not cross cut by deformation  
700 bands and more sinuous slip surfaces. However, large displacement slip surfaces  
701 do cross-cut clusters of deformation bands and more sinuous slip surfaces. This re-  
702 lationship is indicative of a clear evolution of the fault architecture by 1) localizing  
703 displacement and 2) smoothing out slip surfaces.

704 Faults zones with larger offset are associated with larger damage zones and  
705 more slip surfaces. This is particularly telling fact when with the observation that  
706 small displacement slip surface do not cross cut larger displacement slip surfaces.

707 The cross cutting relationship implies that either slip either smaller less con-  
708 tinuous slip surfaces pre-date the onset of the larger offset slip surface or that the  
709 they splay off of it. However, we can reject the former as a possible mechanism as  
710 it does not account for the increased density of slip surfaces on larger offset fault  
711 zones. This implies that they either form directly from the stress heterogeneities  
712 induced by the roughness of larger displacement slip surfaces.

713 Slip surfaces pre-dating large The former case stress heterogeneities from active  
714 slip surfaces induced by fault roughness.

715 faults are smoother than joints or deformation bands

716 At the grains scale, grains are truncated, not ‘plucked’.

717 more linear fault traces where not offset by wavier fault traces

718 **The textural transition between the ultracataclasite and the catacl-**  
719 **asite is best explained by dynamic grain size reduction and wear at the**  
720 **slip surface interface producing ultracataclasite which overprint more**  
721 **diffuse off-fault grain size reduction through grain crushing and defor-**  
722 **mation band production.**

## 723 4 Geometric analysis

### 724 4.1 Method

725 Previous efforts to correlate fault roughness to displacement were frustrated by  
726 limited cliff-size exposure and bad displacement constraints, fundamental to the  
727 quantitative analysis of the roughness data (i.e. [13, 22, 79]). Field methods in this  
728 study correspondingly prioritize 1) slip surface quality 2) good displacement con-  
729 straints 3) the number of faults scanned. Note that we do not necessarily prioritize  
730 large exposure size as has been done in previous work.

731 We collected high precision, high density measurements with optical scanners  
732 in the field and, later, in laboratory on collected hand samples. Every scan was  
733 associated with a constraint on displacement. Moreover, we also recorded the time  
734 of day, location, quality of the slip surface, strike and dip of the fault slip surface,  
735 slickenline rake, and both plan and cross-sectional photographs. When permitted  
736 by outcrop exposure, we recorded an estimate of the fault rock thickness. See  
737 appendix for the tabulation of this data. Together, all these measurements and

738 observations should provide the necessary data to robustly explain and quantify  
739 the processes through which faults mature.

740 **4.1.1 Scan Data Acquisition**

741 A scan of a fault slip surface discretizes it into a *point cloud*, a series of  $x$ ,  $y$   
742 and  $z$  coordinates. We measure slip surface roughness by analysing these point  
743 clouds scans. Specifically, we average the slip parallel and perpendicular spectral  
744 and statistical properties across hundreds of profiles. To ensure the fractal scaling  
745 is well-captured by the point cloud data, we use the following three scanning  
746 instruments capturing various scales of observations: a New View 8000 structure  
747 image analyzer (Zygo Corporation), a NextEngine desktop laser scanner and a  
748 BLAH BLAH LiDAR. Together, these instruments offer the potential to resolve  
749 fault slip surface geometry with high accuracy and precision at over nine decades  
750 of length scale.

751 \*make a map of each areas with the location of every scan encoded with dif-  
752 ferent symbols\*

753 A light detection and ranging instrument was used to resolve length-scales  
754 ranging from meters down to millimetres, (i.e. LiDAR). LiDar has been used in  
755 many previous studies of fault roughness as it is easily deployable in the field and  
756 provides rapid means to collet very large point cloud data set. However, its use is  
757 limiting as it requires exceptionally good and, accordingly, rare exposure of fault  
758 surfaces that are large enough and fresh enough to not have been degraded by  
759 erosion. In this study, we report 5 ??? Lidar Scans (see figure).

760 The bulk of *in situ* field measurements were made at intermediate length-  
761 scales ranging from centimetres down to hundreds of microns with the NextEngine

762 desktop 3D laser scanner. The NextEngine laser scanner has a working distance  
763 of 13 to 57 cm. Maximum accuracy, point cloud density and resolution are all  
764 broadly function of the working distance. In this study nearly all scan where  
765 measure at the optimal minimum working distance (15 cm). Accordingly, point  
766 clouds measured this study are expected to have an accuracy of 0.01 cm and a  
767 point density of 41 540 points/cm<sup>2</sup>. surface both to industrial-grade laser scanner  
768 as reference. The scanner is not exactly built to be field ready. It requires a power  
769 source, low light conditions, a stable surface to sit on, limited dust exposure and  
770 must be connected to a computer. Therefore, to use the scanner in the field, we  
771 connected both the laser scanner and laptop to a solar powered, *Goalzero* battery.  
772 The scanner was encased and padded in a reinforced cardboard box cut such that  
773 the depth exactly corresponds to the optimal instrumental depth of field. The set  
774 up had the added advantage of being very portable, completely removing sunlight  
775 and limiting dust exposure. We report 45 scans using this field apparatus.

776 Finally, hand samples were collected and at McGill laboratories using white  
777 light interferometry. Slip surface samples are cut to be roughly 1 cm<sup>2</sup>. We ap-  
778 ply a 4 nm platinum coating. Point clouds where then produced using the New  
779 View 8000 structure image analyzer (Zygo Corporation). The instrument is an  
780 optical profilometer using a non-contact method, instead using a scanning white  
781 light source. The profilometer can capture surface geometry over length-scales  
782 ranging from millimetres down to hundreds of nanometres by using 2.5, 10 and 50  
783 fold magnification objectives. Point point-clouds are relatively small, however it  
784 is possible to seamlessly stitch smaller scans together. Point clouds where bench-  
785 marked to a silicon carbide mirror reference. For the purpose of this study, all  
786 samples where scanned at 20 and 2.75 magnification objectives. Scans obtained

787 at 20 fold magnification where stitched together to produce sections roughly 2 by  
788 4 millimetres with over  $10^7$  points. Scans obtained at the 2.75 fold magnification  
789 are typically on the order of the sample size and have  $10^6$  points. The later length  
790 scale nicely bridges the interferometry and laser scanner spatial resolution. We  
791 report on 73 point clouds obtained with the white light profilometer.

792 **We assess the effect of erosion of slip surfaces by qualitatively com-**  
793 **paring freshly parted slip surfaces with fault scarps with surfaces that**  
794 **have been exposed to the elements for a long time. Weathered scarps**  
795 **do preserve slip surfaces. However, these have a reddish-brown to dark**  
796 **tarnish and less vitreous lustres. Sections of the slip surface are plucked**  
797 **off. Severely weathered scarps develop a slip perpendicular fabric as-**  
798 **sociated with conjugate fractures and deformation bands abutting into**  
799 **the slip surfaces. These surfaces where not scanned. From our field**  
800 **observation, it is clear that erosion has the effect of re-roughening the**  
801 **slip surfaces, especially at smaller scales. We can confidently attribute**  
802 **these re-roughening effects to erosion because they did not occur in**  
803 **freshly parted slip surfaces. The extent of weathering and erosion was**  
804 **noted and taken into account in post-processing stage on data analysis.**

#### 805 4.1.2 Constraining displacement

806 We associate every scan with displacement constraint. At The Chimney Rock  
807 Fault Array and Big Hole Fault, entire displacement and/or throw profiles have  
808 been measured during previous mapping campaigns ([53, 54, 58, 92]). For the  
809 Chimney Rock fault array, we use geospatial data obtained from Maerten (personal  
810 communications). At big hole we used maps in [92] as reference. At Iron wash,

811 Horse Creek and Molly's Castle, Atilla Aydin's mapping identified clear offset  
812 markers where available ([4]). For these field locations we use maps available in [4].  
813 When necessary base maps for all field locations were digitized and georeferenced  
814 using satellite images. Maps where all used the field to streamline scan data  
815 acquisition. Displacement were estimated after the field campaign using GPS  
816 locations collected in the field. Additional measurements using basic tape measure  
817 and compass triangulation methods where also obtained in the field to obtain true  
818 faults slip surface displacement.

819 Base maps only report stratigraphic throw or, in some cases, offset across fault  
820 zones. However, many slip surfaces, complex networks of deformation bands and  
821 sheared joints which partition offset across fault zone (see figure). We there-  
822 fore make a distinction between *offset* across an entire fault and *displacement*  
823 across a single slip surface. Without good marker horizons and cross-sectional  
824 exposure, how stratigraphic offset is partitioned across slip surfaces is ambiguous.  
825 Offset across the entire fault zone therefore only serves as an upper-bound con-  
826 straint on displacement across a single slip surface slip surface. For 60% of point  
827 cloud measurements, this is the best available constraint on displacement.

828 We were able to reconstruct exact displacement in the following specific cases:  
829 1) if cross sectional exposure indicates only one slip surface; 2) If cross-sectional  
830 exposure is good enough to clearly indicate cutoff surface (lamella, cross-bedding  
831 or lithological contact); or 3) following [25] and, locally, [92], if it is unambiguous  
832 that there is a *principle slip surface* accommodating the overwhelming majority  
833 of fault offset, i.e. it is continuous, it has a layer of fault rock and is unmistakably  
834 more linear and sharp than any other slip surface in the fault zone.

835 Errors on displacement estimates are either reported directly for previous work

836 when available. For Chimney rock, we report  $1m$  precision based on high resolution  
837 GPS mapping by Maerten et al., 2001. For Big Hole, we report  $5m$  precision based  
838 on total station surveying by Shipton et al., 2001. For our field measurements and  
839 those made by Aydin, 1977, we report conservative 10% error on displacement  
840 estimates.

841 **4.1.3 Scan data Processing**

842 We use point cloud spatial statistics to characterize and quantify features of the  
843 topography that could record active surface processes on faults. We developed a  
844 *MatLab* work flow to entirely automate data processing from the raw *.xyz* input  
845 format to the final statistical analysis:

846 1. Preprocessing

- 847 (a) manual inspection and removal of coarsest defects in built in scanner  
848 software
- 849 (b) export point cloud data to *.xyz* data
- 850 (c) Import *.xyz* data into *Matlab*
- 851 (d) Very coarse Height field filter (standard deviation threshold)
- 852 (e) Rotate mean plane to horizontal
- 853 (f) Orient grid along slip direction (using power spectral analysis)
- 854 (g) re-grid to even point spacing
- 855 (h) Remove defects
- 856 i. Remove outliers in the height field (standard deviation threshold)

- 857                   ii. Fractal model filter  
858                   iii. Remove re-gridding artefact

859       2. Processing

- 860           (a) Statistical analysis  
861              i. Scale-dependent *RMS*  
862              ii. Scale-dependent skewness  
863              iii. Scale-dependent kurtosis  
864              iv. Scale-dependent asymmetry  
865           (b) Spectral Analysis  
866              i. Fast Fourier Transform (FFT)  
867              ii. Lomb-Scargle Periodogram

868       *make into figure, include bypasses and other recent additions*

869       Before conducting a statistical analysis scan data must be pre-processed into a  
870       workable format. Scan data is a point cloud - a series of points with coordinates  
871        $x$ ,  $y$  and  $z$ . Scans reported in this study typically have  $10^6$  to  $10^7$  points. In raw  
872       form, the point clouds are randomly oriented, noisy and still contain instrumental  
873       and physical artefacts. Physical artefacts include cracks, eroded sections, and  
874       vegetation; instrumental artefacts include noise, smoothing and scattering. All  
875       these features must be removed. The process of manual removal is labour intensive  
876       and infeasible for a data set of the scope presented in this study. I rather opt to  
877       automate this process. Only very large defects (defects that may substantially  
878       effect the quality of finding a true mean plane) are manually removed.

879        The surface must first be rotated such that the mean plane is horizontal and  
 880        aligned along slip. Linear trends in the data induce unwanted high frequency signal  
 881        in data and also affect the quality of interpolation in upcoming steps. Thus,  $x$ ,  $y$ ,  
 882         $z$  data is rotated around the axis  $\mathbf{u}$  determined by the normalized cross product  
 883        between the normal vector to the mean plane of the point cloud,  $\mathbf{n}$ , and the unit  
 884        vertical vector,  $\mathbf{n}_2$ :

$$\mathbf{u} = \mathbf{n} \times \mathbf{n}_2 / |\mathbf{n} \times \mathbf{n}_2|$$

885        with the rotation,

$$R = \cos \theta \mathbf{I} + \sin \theta [\mathbf{u}]_x + (1 - \cos \theta) \mathbf{u} \otimes \mathbf{u},$$

886        were  $[\mathbf{u}]_x$  is the cross product matrix of  $u$  and  $\otimes$  is the tensor product and  $\mathbf{I}$  is  
 887        the identity matrix.

888        Fault surfaces are anisotropic [56]. The direction of slip is preserved in the  
 889        anisotropy whereby the 'smoothest' direction is slip parallel and the 'roughest'  
 890        direction is perpendicular to slip. The fault scan is rotated around the  $z$  axis such  
 891        that the direction of slip is parallel to the  $x$  axis. The direction of slip is found by  
 892        decimating raw data before performing spectral analysis along directions rotated  
 893        by  $1^\circ$  increments around the z-axis, iterating through the steps of regridding at  
 894        each rotation. In this radial search, roughness is quantified as the integral of the  
 895        log-weighted power spectrum over the entire bandwidth of the sampled surface.  
 896        The direction in which the roughness attains a minimum value is then identified  
 897        as the direction of slip and subsequently used to rotated the original point cloud.  
 898        The data is then interpolated onto a grid using a linear interpolation algorithm.

899 The point spacing of the grid is automatically defined by the point density over  
900 the areal extent of the data:

$$\Delta x = N_{pts}/A \quad (7)$$

901 Where  $\Delta x$  is the point spacing,  $N_{pts}$  is the number of points and  $A$  is the  
902 areal horizontal extent of the data. The later is determined using a convex hull  
903 over the  $x - y$  projection of the point cloud. This treatment results in the point  
904 spacing of the grid to be roughly consistent with that of the original scan.

905 INCLUDE HISTOGRAMS FOR EACH FILTER

906 *Defects* include all physical surface features that are clearly not associated any  
907 faulting process, *e.g.* cracks, eroded patches, vegetation, etc.. Defects are ideneti-  
908 fied and filtered out using combination of thresholding methods. These methods all  
909 involve identifying points or linear segments of points that are statistical outliers  
910 to the distribution characterizing the entire surface.

911 The most aggressive filter implemented searches for outliers to the fractal  
912 model. The filter removes entire linear segments of points with abnormally high  
913 variance in the height field for the given scale of observation. For this implemen-  
914 tation, I iterate over 10 filter segment length-scales. The length-scales are selected  
915 using a log spacing between the 10 points and the length of the entire surface.  
916 The threshold for segment removal is chosen to be four standard deviations from  
917 the mean which accounts for  $< 0.1$  percent of a normal distribution. Note that,  
918 assuming a normal distribution of data for a given scale, the filter does not induce  
919 a systematic bias in the mean value, since the filtering is symmetric around the  
920 mean. However, surface features associated with a truly distinct mechanism of for-

921 mation, in this case cracks and other defects that will typically have much higher  
922 variance, *are* be removed. This general approach ensures that defects, regardless  
923 of their scale are identified and removed.

924 In some cases, abnormally flat sections are introduced into a surface height  
925 field during the interpolation of sparse points. Typically, interpolation on the  
926 edge on a non-convex set of points is subject to this effect. These artefacts are  
927 readily identified following calculation of the surface curvature data. In the log-  
928 transformed absolute value curvature field, these sections appear to be nearly or  
929 exactly zero. The filter rejects point with curvatures less than  $10^{-25}m^{-1}$ . These  
930 values are assumed to be the result of the linear interpolation scheme.

931 Finally, all scan are inspected to make sure that the pre-processing was suc-  
932 cessful. The workflow fails to properly process scans that have too many defects  
933 surface defects. This is because 1) the mean plane is skewed by surface defects  
934 and in turn affects identifications of outliers in the height-field; and 2) the dis-  
935 tinction between the fault surface and outliers becomes less distinct in the fractal  
936 model. These scans were manually cleaned and oriented before re-processing them.  
937 Manual changes were executed in a point cloud editing software *CloudCompare*.

938 Pre-processed scans are  $N$  by  $M$  scalar fields of fault surface topography(the  
939 sitance from the mean plane) aligned with slip along the  $x$  axis. NaN values mark  
940 locations where data is missing or was removed by filters. Point spacing is defined  
941 the mean point density of the scan in the  $x$ - $y$  plane.

942 We adapt the general pre-processing workflow to account for instrumental arte-  
943 facts. Scans collected with the LiDAR required more extensive manual point re-  
944 moval to avoid features such as vegetation, spurious outlier and large defects to  
945 affect the quality of the preprocessing. Scans collected at the intermediate scale

946 with the laser scanner easily followed this workflow. Finally, scan collected with  
947 the white light interferometer have little to no surface defects and are aligned  
948 before scanning. Moreover, instrumental *Zygo* software automatically generates  
949 point clouds in grid-form. Therefore, for these scans, most of the pre-processing  
950 step are omitted.

951 **4.1.4 Statistical Analysis**

952 After pre-processing, scans discretize defect-free slip surfaces with grids with rows  
953 aligned with the slip direction. We compute the power spectral density content for  
954 every continuous segment of every single profile of the grid using a Fast Fourier  
955 Transform (FFT). Individual spectra are interpolated onto a master frequency  
956 vector. For a given frequency, the distribution of power values across the pro-  
957 files through along the slip is strongly skewed (see figure xxx). The skewness is  
958 attributable to the non-negative constraint on power and residual outlying pro-  
959 files (defects not properly removed). To provide a more representative and robust  
960 measure of maximum likelihood, we use the geometrical mean instead of the arith-  
961 metical mean. Accordingly, errors represent the  $1\sigma$  range in the log-transformed  
962 distribution. The analysis yields one representative spectrum for each scan.

963 The spatial frequency content of slip surfaces follow a power law. This charac-  
964 teristic is roughly fixed for a single slip surface regardless of the scale sampled in  
965 our instrumental array. Fixed scaling and its power law form in frequency space is  
966 a feature of the fractal character of fault surfaces. We can thus further distil the  
967 roughness measurements using the fractal model of the fault:

$$P(k) = Ck^{-\beta} \quad (8)$$

Accordingly the entire spectral information of a scan can be summarized with the prefactor ( $C$ ) and the scaling exponent ( $\beta$ ). Determining fractal parameters from spectra is not trivial. *A priori*, the fractal model is determined using a weighted power law regression through the spectra. Weights are determined according to the inverse  $1\sigma^2$  variance of the power estimates. However, confidence interval on the fit parameters are strongly sensitive to both instrumental and analytical biases (XXX schittbulh 1998). Biases induce unwanted high or low pass filters in the spectral content-amplifying or diminishing selective bandwidth. The combination of instruments and highly overlapping bandwidths provides a means to identify the affected sections and suppress methodological bias. The comparison of the power law fit through multiple heavily overlapping instrumental bandwidths to the representative spectral of individual scans highlights instrument-specific biases. In doing so, we identify conservative bounds on sections of frequency spectrum that deviated from the power law fit. For our instruments, we find that artefacts are particularly disruptive at the small scale instrumental limit. The LiDar and laser scanner are dominated by a shallower slope at the high frequency tail of the spectra which has been interpreted in previous studies as random noise (XXX). Conversely, the spectra of the scan collected using the white light interferometer have steeper high frequency tails. This artefact has not been reported in previous studies in spite of the extensive use of the instrument. This discrepancy is likely attributable to the comparatively limited and subdued use of aggressive smoothing filters both in the scan data and in the spectra our analysis. Affected bandwidths are omitted from subsequent analysis. In spite of this approach, small discrepancies in parametrization of the power law fit for a given slip surface render the extrapolation of measurements from on instrumental bandwidth to the other

993 instrumental scale of limited use. We therefore choose to report any further re-  
994 sults at the bandwidth or specific wavelength best captured by the instrumental  
995 magnification.

996 INCLUDE A FIGURE WITH: ORIGINAL SURFACE, AUTOMATICALLY  
997 PROCESSED GRID, MANUALLY PROCESSED GRID AND CORRESPOND-  
998 ING POWER SPECTRA.

999 identifying fractal scaling section plot of white light all magnifications compu-  
1000 tational scheme to select the good section error on direct displacement estimates?

## 1001 4.2 Results

### 1002 4.2.1 Roughness measurements

1003 figures to include:

- 1004 • all spectra  
1005 • increasing anisotropy (two surfaces) - polar plot

1006 Figure XXX shows the all the PSD calculations obtained from the scans col-  
1007 lected in this study. Consistent with previous work, we find that the PSD spectra  
1008 over the entire bandwidth reported in this study generally follow a power law scal-  
1009 ing (a linear relation in log-log space). This feature corresponds to the constant  
1010 fractal scaling. The scaling exponent and pre-factors are calculated using linear  
1011 least-squares fit of the spectra in log-log space. The Hurst exponent can then be  
1012 obtained according to equation XXX.

1013 In the slip perpendicular direction, Hurst exponents range from XXX to XXX,  
1014 with an average value of 0.8ish; Prefactors range from XXX to XXX with an

average value of XXX. In the slip parallel direction, Hurst exponents range from XXX to XXX, with an average value of 0.8ish; Prefactors range from XXX to XXX with an average value of XXX. Implicit to the pre-processing grid alignment, for any single scan the slip parallel direction is systematically smoother than the slip perpendicular direction indicating a clear surface anisotropy. The entire data set does however indicate an overlapping range in slip parallel and perpendicular directions. We also note that lower pre-factors are generally associated with lower Hurst exponents.

An evolution with displacement is weakly expressed in the spectral analysis but is cluttered and obscured by highly variable errors on displacements and roughness measurements. In order to highlight the effect of displacement on the surface roughness, we separate our scan data into two distinct populations. 1) Scan data with direct displacement constraint and 2) scan data associated with maximum displacement constraints. Brodsky et al., 2011, tested the validity of a power law relation between fault roughness at various specific scales and displacement. Building upon this approach, we use both data populations to test the validity and parametrization of the fit and the Implicit hypothesis that faults smooth as a function of displacement—the smoothing model. Scan data with direct displacement constraints serves as a direct test and a means to parametrize the smoothing model. For the model to be valid it must agree with further constraints imposed by data with only maximum displacement estimates.

A point defined by the maximum error bound on displacement and the roughness of the fault surface is in agreement with smoothing model if it is rougher than roughness prescribed by the model as parametrized by direct measurement. Conversely, if the point is rougher than the model prediction, it is not physically

1040 possible in the model construct. A null hypothesis would prescribe no bound on  
1041 the roughness and would simply have the predicted roughness of a fault be defined  
1042 by the probability distribution function of the entire roughness dataset.

1043 \* probably will revisit this \*

1044 Accordingly, we can roughly estimate the probability that our distribution of  
1045 data relative to the smoothing model is a random element of chance according to:

$$P = \prod p(y_i > Y(x_i)) \quad (9)$$

1046

---

1047 Figures XXX to XXX shows the relation between roughness and displacement  
1048 as interpolated a various scales of observation. Vertical error bars on the power  
1049 spectral density are obtained from the confidence interval of the of the fractal  
1050 model regression. Horizontal errorbars on displacement are defined on a case by  
1051 case basis from field observations and previous work in on the fault arrays. We  
1052 present both the fit through the our entire dataset (comprised of direct and up-  
1053 per bound constraints on displacement) and through the the directly constrained  
1054 displacement estimates. Fits are obtained using a least squares linear regression  
1055 through the log-transformed data sets. In order to provide error bounds on the  
1056 fit parameters, we use a full Monte Carlo simulation sampling direct displacement  
1057 estimated as Gaussian distributions, upper bound displacement constrains as com-  
1058 pletely random distributions across the entire possible range of displacements and  
1059 power spectral density estimates as log normal distributions. Errors represent on  
1060 standard deviation estimated from 10000 simulations.

1061 The weak trend across the entire dataset imply and expectation of smoother

1062 slip surfaces in fault zones which have accommodated larger displacement.

1063 Conversely the stronger trend across the well constrained data implies that an  
1064 individual slip surface smooths with displacement. The smoothing exponent varies  
1065 according to the different scales of observation (XXX at the laser at the centimeter  
1066 scale, XXX at the milimeter scale and XXX at the micron scale). While a power  
1067 law fit to the best constrained measurements is has poor fit metrics, we find a nearly  
1068 perfect agreement with roughness measurements only associated with upper bound  
1069 constraints.

1070 Two constraints on displacement – two data populations plot of all the spectra  
1071 color coded with displacement smoothing plots: parallel - $\zeta$  all scales perpendicular  
1072 - $\zeta$  all scales Hurst exponent - $\zeta$  all scales Fit for smoothing through direct data,  
1073 discuss consistency with max disp data Other statistical metrics? Poly-gaussian  
1074 features in the surface roughness Skewness of height field as a function of scale  
1075 Null result worth reporting? Do a plot of the evolution of skewness at the grain  
1076 scale?

1077 qualitative illustration of maturity

### 1078 4.3 Hard facts

1079 The following is a list of ‘hard facts’ that can be established from the both the  
1080 qualitative and quantitative data:

- 1081 • faults are smoother than joints or deformation bands
  - 1082 – power spectrum shows that fault slip surfaces are systematically smoother  
1083 than joint and deformation band surfaces at all wave lengths reported  
1084 in this study ( $10^{-6}$  to  $10^5$  meters)

- 1085 • At the grains scale, grains are truncated, not ‘plucked’.
- 1086 • The roughness of a slip surface is sensitive to its displacement history. This  
1087 result is robust across multiple faults both nucleated from deformation bands  
1088 and joints and variations in fault rock and host rock lithology.
- 1089 • The smoothing exponent is likely more than 1 at certain scales - quote from  
1090 Emily: “In all of these cases, the scatter of the data is large, but the basic  
1091 result holds: the absolute value of the exponent is much less than 1.”
- 1092 • The smoothing rate is highest at small displacements and decreases with  
1093 displacement.
- 1094 • Smoothing occurs at all scales of this study
  - 1095 • a slip surface from a large offset fault is more likely to be smoother
  - 1096 • for any given the displacement on a fault, the smoothest slip surface roughly  
1097 follows the same smoothing trend as that defined by direct displacement  
1098 measurements.
- 1099 • The roughness varies spatially on a slip surface - the scatter in the data  
1100 exceeds the instrumental error
- 1101 • the height distribution of points on a slip surface can be far from normally  
1102 distributed.
- 1103 • the Hurst exponent has a very large range in values (less than Zero to 0.9)
- 1104 • more linear fault traces where not offset by wavier fault traces

<sub>1105</sub> **5 Model**

<sub>1106</sub> In this study, we utilize work minimization and boundary element numerical mod-  
<sub>1107</sub> elling to capture the growth of fault damage and the effect of rough asperities.  
<sub>1108</sub> The modelling component is motivated by the following questions: can geomet-  
<sub>1109</sub> rical asperities fail through shear? In so doing, how do they fail?—and what are  
<sub>1110</sub> its sensitivities to asperity geometry and strength? Does strength heterogeneity  
<sub>1111</sub> and mechanical wear by the truncation of asperities properly capture the evolu-  
<sub>1112</sub> tion of fault slip surfaces with displacement. These questions prompt the need for  
<sub>1113</sub> physically robust models that can be accomodating of complex fault or asperity  
<sub>1114</sub> geometries. The complexity of these geometries imply that off fault damage will  
<sub>1115</sub> grow in complex stress conditions— conditions that are currently poorly captured  
<sub>1116</sub> by simple analytical solutions (e.g. [27]). Moreover, complexities related to the  
<sub>1117</sub> discontinuous nature of fracture are more simply captured by boundary element  
<sub>1118</sub> modelling than existing finite element or finite difference models. This simplicity  
<sub>1119</sub> arises from need of fewer, less sparse, sets of equations to solve ([33]). Limita-  
<sub>1120</sub> tions of the boundary elements approach for fault modelling and off fault damage  
<sub>1121</sub> predictions is the difficulty of accumulating offset. Maximum allowable offset is  
<sub>1122</sub> roughly half the length of boundary elements. Along with this complications is the  
<sub>1123</sub> implicit trade off between model resolution and displacement. Approaches can be  
<sub>1124</sub> taken to circumvent the challenge however its development and implementation  
<sub>1125</sub> are beyond the current scope of this study.

<sub>1126</sub> The model builds off of fric2D and growth by optimization of work (GROW)  
<sub>1127</sub> developed by Michele Cooke and Jessica McBeck. Fric2D solves for displacement  
<sub>1128</sub> and stress conditions on fault elements with prescribed constitutive behaviours

given prescribed boundary element stress boundary conditions and material properties in two dimensions. Constitutive behaviour of fault elements are defined by its static and dynamic friction, critical slip distance, and shear and normal stiffness. In turn the behaviour of the medium fault elements and boundary elements is linear elastic defined by Poisson's ratio and Young's modulus. For its part, GROW predicts fracture propagation paths. It does so by minimizing the external work on a system. As a natural analogue, the external work is the tectonic work imposed on a fault and its fault blocks, together comprising the system. The model allows for the simultaneous growth of multiple fractures. The general algorithm uses the same boundary element method as fric2D to describe the fractures–linear dislocation elements that discretize the entire length of the fault. As a crack grows, dislocation elements are added radially to the tip of the crack so as to minimize the external work on the system normalized by the crack area ( $W_{ext}/\Delta A$ ). External work is further defined as:

$$W_{ext} = \oint (\tau u_s + \sigma_n u_n) dB \quad (10)$$

External work is readily calculated from the output of fric2D. Accordingly it is possible to iteratively test a range of directions of growth, compare the external work required, and choose the energetically preferred direction of crack growth. This process continues until stress at the tip of the cracks is not sufficient to overcome the fracture toughness. Therein lies the general algorithm of GROW.

In practice GROW utilizes almost the same inputs as fric2D. The user must specify what points are considered to be 'flaws'. Only the coordinates associated with the flaws are analysed and allowed to grow according to the GROW algorithm.

1151 The computational cost of multiple initiation points is large. Every added flaw  
 1152 grows the computational cost exponentially according to the angular range and  
 1153 resolution. We rather use fric2D to educate the choice of coordinated for the flaws  
 1154 on the fault.

1155 Stress conditions are assessed along the fault elements. Normal ( $\sigma_{11}$ ), shear  
 1156 ( $\sigma_{12} = \sigma_{21}$ ) and tangential ( $\sigma_{22}$ ) stresses on the fault elements yield the two di-  
 1157 mensional stress tensor. Its Eigenvalues in turn allow for the determinations of  
 1158 principle stresses ( $\sigma_1$  and  $\sigma_3$ ). These in turn allow for calculation of the Mohr  
 1159 Coulomb stress and the assessment of elements prone to failure in shear according  
 1160 to host rocks angle of internal friction ( $\phi$ ) and cohesion ( $c$ ).

$$\tau_m = \sigma_m \sin(\phi) + c \cos(\phi) \quad (11)$$

1161 where,

$$\tau_m = \frac{\sigma_1 - \sigma_3}{2} \quad (12)$$

1162 and,

$$\sigma_m = \frac{\sigma_1 + \sigma_3}{2}. \quad (13)$$

1163 We also assess element that may fail in tension. Elements with least principle  
 1164 stress in tension exceeding the cohesive strength of the medium are also identified  
 1165 as being prone to fail. In the likely case that entire fault segments (multiple fault  
 1166 elements) are in stress conditions exceeding the failure criterion of the rock, we  
 1167 choose local maxima of Coulomb stress and tensile stress along these segments as  
 1168 the failure points.

1169 This additional functionality is implemented in Matlab and seamlessly links  
1170 fric2d, failure assessments and GROW into one single workflow.

1171 **5.1 Model Results**

1172 **6 Discussion**

1173 **6.0.1 Tying the model together with roughness measurements and**  
1174 **model**

1175 wear rate (character), tying together model with

1176 **6.1 An external estimate of gouge production and fault**  
1177 **thickness \* this section will likely be removed**

1178 The data collected in this study offers the unique opportunity to provide new  
1179 indirect estimates of fault rock production, fault thickness and dilation rate over  
1180 an entire fault. We know that 1) the primordial roughness is systematically rougher  
1181 than mature faults, 2) the primordial roughness is relatively constant, and 3) the  
1182 roughness can be estimated for a given displacement. Using these results, I will  
1183 estimate the volume of fault rock produced through wear and the corresponding  
1184 roughness induced accommodation space in the fault system.

1185 Displacing two rough fractal surface in shear requires dilation. The expectation  
1186 dilation can be estimated according to the amplitude of the largest wavelength ( $\lambda$ )  
1187 being offset (see figure XXX). For a given displacement,  $u$ , the largest wavelength  
1188 in the system will be  $\lambda = 2u_i$ . Using a fractal paradigm to define the average  
1189 amplitude of a given wavelength according to the pre-factor  $\beta$  and the Hurst

<sub>1190</sub> scaling exponent,  $H$ , (\*reference the equation\*) we find that the dilation,  $A$  can  
<sub>1191</sub> be expressed as a function of displacement:

$$A(u) = \sqrt{\beta 2u^{-2H-1}} \quad (14)$$

<sub>1192</sub> If we apply this to an entire fault system with displacement field,  $U$ , we can  
<sub>1193</sub> estimate the void space that would be produced:

$$V_{void}(U) = \int_S \sqrt{\beta 2U^{-2H-1}} dS \quad (15)$$

<sub>1194</sub> Since the fault system is closed any change in fault roughness *must* be coupled  
<sub>1195</sub> to the fault core. If all changes in the fault surface are associated with a production  
<sub>1196</sub> of fault rock, we can effectively estimate the volume of fault rock that has been  
<sub>1197</sub> produced from displacement  $u_0$  to  $u_f$  by comparing the volume integral under the  
<sub>1198</sub> corresponding initial and final slip surfaces  $S(u_0)$  and  $S(u_f)$ .

$$\frac{\Delta V_{faultrock}}{\Delta u} = \int_S S(u_0) - S(u_f) dS \quad (16)$$

<sub>1199</sub> volume integral under the surfaces,  $S$ , can be estimated numerically according  
<sub>1200</sub> to the frequency distribution prescribed by the RMS the entire fault system. Note  
<sub>1201</sub> that the RMS is estimated at the length scale of the entire fault; wear processes  
<sub>1202</sub> are active at all length scales below this.

$$\int S dS \approx \quad (17)$$

<sub>1203</sub> Now for the displacement field,  $U$ , we can estimate the total fault rock produced  
<sub>1204</sub> by using the primordial surface roughness,  $S(0)$ , and the prediction of the surface

1205 roughness extrapolated to the length of the fault (\* reference the the equation of  
1206 smoothing \*) such that:

$$V_{fauitrock}(U) = \int_S S(0) - S(U) dS \quad (18)$$

1207 The comparison between the two quatities is telling. If the amount of fault  
1208 rock is

## 1209 7 conclusion

### 1210 7.1 future work

## 1211 References

- 1212 [1] Keiiti Aki. Asperities, barriers, characteristic earthquakes and strong motion  
1213 prediction. *Journal of Geophysical Research: Solid Earth*, 89(B7):5867–5872,  
1214 1984.
- 1215 [2] JeFoa Archard. Contact and rubbing of flat surfaces. *Journal of applied  
1216 physics*, 24(8):981–988, 1953.
- 1217 [3] CA Aviles, CH Scholz, and John Boatwright. Fractal analysis applied to  
1218 characteristic segments of the san andreas fault. *Journal of Geophysical  
1219 Research: Solid Earth*, 92(B1):331–344, 1987.
- 1220 [4] Atilla Aydin. *Faulting in sandstone*. PhD thesis, Stanford, 1977.

- 1221 [5] Atilla Aydin and Arvid M Johnson. Development of faults as zones of defor-  
1222 mation bands and as slip surfaces in sandstone. *Pure and applied Geophysics*,  
1223 116(4):931–942, 1978.
- 1224 [6] Nir Badt, Yossef H Hatzor, Renaud Toussaint, and Amir Sagy. Geometrical  
1225 evolution of interlocked rough slip surfaces: The role of normal stress. *Earth*  
1226 and *Planetary Science Letters*, 443:153–161, 2016.
- 1227 [7] Philip Berger and Arvid M Johnson. First-order analysis of deformation of  
1228 a thrust sheet moving over a ramp. *Tectonophysics*, 70(3-4):T9–T24, 1980.
- 1229 [8] RL Biegel, W Wang, CH Scholz, and GN BorrNoTr. 1. effects of surface  
1230 roughness on initial friction and slip hardening in westerly granite. *Journal*  
1231 of *Geophysical Research*, 97(B6):8951–8964, 1992.
- 1232 [9] Andrea Bistacchi, W Ashley Griffith, Steven AF Smith, Giulio Di Toro,  
1233 Richard Jones, and Stefan Nielsen. Fault roughness at seismogenic depths  
1234 from lidar and photogrammetric analysis. *Pure and Applied Geophysics*,  
1235 168(12):2345–2363, 2011.
- 1236 [10] Tom G Blenkinsop. Thickness—displacement relationships for deformation  
1237 zones: Discussion. *Journal of Structural Geology*, 11(8):1051–1053, 1989.
- 1238 [11] Elisabeth Bouchaud. Scaling properties of cracks. *Journal of Physics: Con-*  
1239 *densed Matter*, 9(21):4319, 1997.
- 1240 [12] Frank Philip Bowden and David Tabor. *The friction and lubrication of solids*,  
1241 volume 1. Oxford university press, 2001.

- 1242 [13] Emily E Brodsky, Jacquelyn J Gilchrist, Amir Sagy, and Cristiano Collettini.  
1243 Faults smooth gradually as a function of slip. *Earth and Planetary Science*  
1244 *Letters*, 302(1):185–193, 2011.
- 1245 [14] Emily E Brodsky, James D Kirkpatrick, and Thibault Candela. Constraints  
1246 from fault roughness on the scale-dependent strength of rocks. *Geology*,  
1247 44(1):19–22, 2016.
- 1248 [15] Stephen R Brown and Christopher H Scholz. Broad bandwidth study of the  
1249 topography of natural rock surfaces. *J. geophys. Res.*, 90(B14):12575–12582,  
1250 1985.
- 1251 [16] Roland Bürgmann, David D Pollard, and Stephen J Martel. Slip distribu-  
1252 tions on faults: effects of stress gradients, inelastic deformation, heteroge-  
1253 neous host-rock stiffness, and fault interaction. *Journal of Structural Geol-*  
1254 *ogy*, 16(12):1675–1690, 1994.
- 1255 [17] J Byerlee. Friction, overpressure and fault normal compression. *Geophysical*  
1256 *Research Letters*, 17(12):2109–2112, 1990.
- 1257 [18] Jonathan Saul Caine, James P Evans, and Craig B Forster. Fault zone  
1258 architecture and permeability structure. *Geology*, 24(11):1025–1028, 1996.
- 1259 [19] Thibault Candela and Emily E Brodsky. The minimum scale of grooving on  
1260 faults. *Geology*, 44(8):603–606, 2016.
- 1261 [20] Thibault Candela, François Renard, Michel Bouchon, Alexandre Brouste,  
1262 David Marsan, Jean Schmittbuhl, and Christophe Voisin. Characterization  
1263 of fault roughness at various scales: Implications of three-dimensional high

- 1264 resolution topography measurements. *Mechanics, Structure and Evolution*  
1265 *of Fault Zones*, pages 1817–1851, 2010.
- 1266 [21] Thibault Candela, François Renard, Michel Bouchon, Jean Schmittbuhl, and  
1267 Emily E Brodsky. Stress drop during earthquakes: effect of fault roughness  
1268 scaling. *Bulletin of the Seismological Society of America*, 101(5):2369–2387,  
1269 2011.
- 1270 [22] Thibault Candela, François Renard, Yann Klinger, Karen Mair, Jean Schmit-  
1271 tbuhl, and Emily E Brodsky. Roughness of fault surfaces over nine decades  
1272 of length scales. *Journal of Geophysical Research: Solid Earth*, 117(B8),  
1273 2012.
- 1274 [23] Thibault Candela, François Renard, Jean Schmittbuhl, Michel Bouchon, and  
1275 Emily E Brodsky. Fault slip distribution and fault roughness. *Geophysical*  
1276 *Journal International*, 187(2):959–968, 2011.
- 1277 [24] G Chambon, J Schmittbuhl, A Corfdir, N Orellana, M Diraison, and  
1278 Y Géraud. The thickness of faults: From laboratory experiments to field  
1279 scale observations. *Tectonophysics*, 426(1):77–94, 2006.
- 1280 [25] FM Chester and JM Logan. Implications for mechanical properties of brittle  
1281 faults from observations of the punchbowl fault zone, California. *Pure and*  
1282 *Applied Geophysics*, 124(1-2):79–106, 1986.
- 1283 [26] FM Chester and JM Logan. Composite planar fabric of gouge from the  
1284 punchbowl fault, California. *Journal of Structural Geology*, 9(5-6):621IN5–  
1285 634IN6, 1987.

- 1286 [27] Frederick M Chester and Judith S Chester. Stress and deformation along  
1287 wavy frictional faults. *Journal of Geophysical Research: Solid Earth*,  
1288 105(B10):23421–23430, 2000.
- 1289 [28] Frederick M Chester, James P Evans, and Ronald L Biegel. Internal structure  
1290 and weakening mechanisms of the san andreas fault. *Journal of Geophysical  
1291 Research: Solid Earth*, 98(B1):771–786, 1993.
- 1292 [29] Judith S Chester and Raymond C Fletcher. Stress distribution and failure  
1293 in anisotropic rock near a bend on a weak fault. *Journal of Geophysical  
1294 Research: Solid Earth*, 102(B1):693–708, 1997.
- 1295 [30] Michele L Cooke. Fracture localization along faults with spatially varying  
1296 friction. *Journal of Geophysical Research: Solid Earth*, 102(B10):22425–  
1297 22434, 1997.
- 1298 [31] ML Cooke and DD Pollard. Bedding-plane slip in initial stages of fault-  
1299 related folding. *Journal of Structural Geology*, 19(3-4):567–581, 1997.
- 1300 [32] Patience A Cowie and Zoe K Shipton. Fault tip displacement gradients and  
1301 process zone dimensions. *Journal of Structural Geology*, 20(8):983–997, 1998.
- 1302 [33] Steven L Crouch and AM Starfield. *Boundary element methods in solid  
1303 mechanics: with applications in rock mechanics and geological engineering*.  
1304 Allen & Unwin, 1982.
- 1305 [34] NC Davatzes and A Aydin. Distribution and nature of fault architecture in  
1306 a layered sandstone and shale sequence: An example from the moab fault,  
1307 utah. 2005.

- 1308 [35] Nicholas C Davatzes, Atilla Aydin, and Peter Eichhubl. Overprinting fault-  
1309       ing mechanisms during the development of multiple fault sets in sandstone,  
1310       chimney rock fault array, utah, usa. *Tectonophysics*, 363(1):1–18, 2003.
- 1311 [36] Guy Davidesko, Amir Sagy, and Yossef H Hatzor. Evolution of slip surface  
1312       roughness through shear. *Geophysical Research Letters*, 41(5):1492–1498,  
1313       2014.
- 1314 [37] James H Dieterich and Deborah Elaine Smith. Nonplanar faults: Mechanics  
1315       of slip and off-fault damage. In *Mechanics, Structure and Evolution of Fault*  
1316       *Zones*, pages 1799–1815. Springer, 2009.
- 1317 [38] Eric M Dunham, David Belanger, Lin Cong, and Jeremy E Kozdon. Earth-  
1318       quake ruptures with strongly rate-weakening friction and off-fault plasticity,  
1319       part 2: Nonplanar faults. *Bulletin of the Seismological Society of America*,  
1320       101(5):2308–2322, 2011.
- 1321 [39] James T Engelder. Cataclasis and the generation of fault gouge. *Geological*  
1322       *Society of America Bulletin*, 85(10):1515–1522, 1974.
- 1323 [40] James P Evans. Thickness-displacement relationships for fault zones. *Jour-*  
1324       *nal of structural geology*, 12(8):1061–1065, 1990.
- 1325 [41] Zijun Fang and Eric M Dunham. Additional shear resistance from fault  
1326       roughness and stress levels on geometrically complex faults. *Journal of Geo-*  
1327       *physical Research: Solid Earth*, 118(7):3642–3654, 2013.
- 1328 [42] Haakon Fossen and Jonny Hesthammer. Deformation bands and their sig-  
1329       nificance in porous sandstone reservoirs. *First Break*, 16(1):21–25, 1998.

- 1330 [43] Haakon Fossen, Tord Erlend Skeie Johansen, Jonny Hesthammer, and  
1331 Atle Rotevatn. Fault interaction in porous sandstone and implications  
1332 for reservoir management; examples from southern utah. *AAPG bulletin*,  
1333 89(12):1593–1606, 2005.
- 1334 [44] Haakon Fossen, Richard A Schultz, Zoe K Shipton, and Karen Mair. De-  
1335 formation bands in sandstone: a review. *Journal of the Geological Society*,  
1336 164(4):755–769, 2007.
- 1337 [45] JA Greenwood and JBP Williamson. Contact of nominally flat surfaces. In  
1338 *Proceedings of the Royal Society of London A: Mathematical, Physical and*  
1339 *Engineering Sciences*, volume 295, pages 300–319. The Royal Society, 1966.
- 1340 [46] W Ashley Griffith, Stefan Nielsen, Giulio Di Toro, and Steven AF Smith.  
1341 Rough faults, distributed weakening, and off-fault deformation. *Journal of*  
1342 *Geophysical Research: Solid Earth*, 115(B8), 2010.
- 1343 [47] Christopher Harbord, Stefan Nielsen, and Nicola De Paola. Fault zone rough-  
1344 ness controls slip stability. In *EGU General Assembly Conference Abstracts*,  
1345 volume 18, page 9799, 2016.
- 1346 [48] Rebecca M Harrington and Emily Brodsky. Smooth, mature faults radiate  
1347 more energy than rough, immature faults in parkfield, ca. *Bulletin of the*  
1348 *Seismological Society of America*, 99(4):2323–2334, 2009.
- 1349 [49] RR Jones, S Kokkalas, and KJW McCaffrey. Quantitative analysis and  
1350 visualization of nonplanar fault surfaces using terrestrial laser scanning (li-  
1351 dar)—the arkitsa fault, central greece, as a case study. *Geosphere*, 5(6):465–  
1352 482, 2009.

- 1353 [50] Vincent Cooper Kelley and N James Clinton. *Fracture systems and tectonic*  
1354       *elements of the Colorado Plateau*. Number 6-7. University of New Mexico  
1355       Press, 1960.
- 1356 [51] Bill Kilsdonk and Raymond C Fletcher. An analytical model of hanging-wall  
1357       and footwall deformation at ramps on normal and thrust faults. *Tectono-*  
1358       *physics*, 163(1-2):153–168, 1989.
- 1359 [52] S Kokkalas, RR Jones, KJW McCaffrey, and P Clegg. Quantitative fault  
1360       analysis at arkitsa, central greece, using terrestrial laser-scanning (lidar).  
1361       *Bulletin of the Geological Society of Greece*, 37:1–14, 2007.
- 1362 [53] Robert W Krantz. Orthorhombic fault patterns: the odd axis model and  
1363       slip vector orientations. *Tectonics*, 8(3):483–495, 1989.
- 1364 [54] RW Krantz. Orthorhombic fault patterns and three-dimensional strain anal-  
1365       ysis, northern san rafael swell, utah. In *Geological Society of America Ab-*  
1366       *stracts with Programs*, volume 18, page 125, 1986.
- 1367 [55] Thorne Lay, Hiroo Kanamori, and Larry Ruff. *The asperity model and the*  
1368       *nature of large subduction zone earthquakes*. na, 1982.
- 1369 [56] Joong-Jeek Lee and Ronald L Bruhn. Structural anisotropy of normal fault  
1370       surfaces. *Journal of Structural Geology*, 18(8):1043–1059, 1996.
- 1371 [57] Alan V Levy and Nancy Jee. Unlubricated sliding wear of ceramic materials.  
1372       *Wear*, 121(3):363–380, 1988.

- 1373 [58] Laurent Maerten, David D Pollard, and Frantz Maerten. Digital mapping of  
1374 three-dimensional structures of the chimney rock fault system, central utah.  
1375 *Journal of Structural Geology*, 23(4):585–592, 2001.
- 1376 [59] Benoit B Mandelbrot. Self-affine fractals and fractal dimension. *Physica*  
1377 *scripta*, 32(4):257, 1985.
- 1378 [60] Benoit B Mandelbrot, Dann E Passoja, and Alvin J Paullay. Fractal char-  
1379 acter of fracture surfaces of metals. 1984.
- 1380 [61] Jessica A McBeck, Elizabeth H Madden, and Michele L Cooke. Growth by  
1381 optimization of work (grow): A new modeling tool that predicts fault growth  
1382 through work minimization. *Computers & Geosciences*, 88:142–151, 2016.
- 1383 [62] KR McClay and PG Ellis. Analogue models of extensional fault geometries.  
1384 *Geological Society, London, Special Publications*, 28(1):109–125, 1987.
- 1385 [63] Brendan J Meade. Algorithms for the calculation of exact displacements,  
1386 strains, and stresses for triangular dislocation elements in a uniform elastic  
1387 half space. *Computers & geosciences*, 33(8):1064–1075, 2007.
- 1388 [64] HC Meng and KC Ludema. Wear models and predictive equations: their  
1389 form and content. *Wear*, 181:443–457, 1995.
- 1390 [65] MS Moreno, J Bolte, J Klotz, and Dr Melnick. Impact of megathrust ge-  
1391 ometry on inversion of coseismic slip from geodetic data: Application to the  
1392 1960 chile earthquake. *Geophysical Research Letters*, 36(16), 2009.
- 1393 [66] Rodrick Dane Myers. *Structure and hydraulics of brittle faults in sandstone*.  
1394 PhD thesis, Stanford University, 1999.

- 1395 [67] Yoshimitsu Okada. Internal deformation due to shear and tensile faults in  
1396 a half-space. *Bulletin of the Seismological Society of America*, 82(2):1018–  
1397 1040, 1992.
- 1398 [68] Paul G Okubo and James H Dieterich. Effects of physical fault properties on  
1399 frictional instabilities produced on simulated faults. *Journal of Geophysical*  
1400 *Research: Solid Earth*, 89(B7):5817–5827, 1984.
- 1401 [69] Kenshiro Otsuki, Nobuaki Monzawa, and Toshiro Nagase. Fluidization and  
1402 melting of fault gouge during seismic slip: Identification in the nojima fault  
1403 zone and implications for focal earthquake mechanisms. *Journal of Geophys-*  
1404 *ical Research: Solid Earth*, 108(B4), 2003.
- 1405 [70] Andrew Clell Palmer and JR Rice. The growth of slip surfaces in the pro-  
1406 gressive failure of over-consolidated clay. In *Proceedings of the Royal Society*  
1407 *of London A: Mathematical, Physical and Engineering Sciences*, volume 332,  
1408 pages 527–548. The Royal Society, 1973.
- 1409 [71] William L Power and Terry E Tullis. Euclidean and fractal models for the  
1410 description of rock surface roughness. *Journal of Geophysical Research: Solid*  
1411 *Earth*, 96(B1):415–424, 1991.
- 1412 [72] William L Power, Terry E Tullis, and John D Weeks. Roughness and  
1413 wear during brittle faulting. *Journal of Geophysical Research: Solid Earth*,  
1414 93(B12):15268–15278, 1988.
- 1415 [73] WL Power, TE Tullis, SR Brown, GN Boitnott, and CH Scholz. Roughness  
1416 of natural fault surfaces. *Geophysical Research Letters*, 14(1):29–32, 1987.

- 1417 [74] CA Queener, TC Smith, and WL Mitchell. Transient wear of machine parts.  
1418     *Wear*, 8(5):391–400, 1965.
- 1419 [75] François Renard, Christophe Voisin, David Marsan, and Jean Schmittbuhl.  
1420     High resolution 3d laser scanner measurements of a strike-slip fault quan-  
1421     tify its morphological anisotropy at all scales. *Geophysical Research Letters*,  
1422     33(4), 2006.
- 1423 [76] Elizabeth Ritz, David D Pollard, and Michael Ferris. The influence of fault  
1424     geometry on small strike-slip fault mechanics. *Journal of Structural Geology*,  
1425     73:49–63, 2015.
- 1426 [77] Eugene C Robertson et al. Continuous formation of gouge and breccia dur-  
1427     ing fault displacement. In *The 23rd US Symposium on Rock Mechanics*  
1428     (*USRMS*). American Rock Mechanics Association, 1982.
- 1429 [78] Amir Sagy and Emily E Brodsky. Geometric and rheological asperities in an  
1430     exposed fault zone. *Journal of Geophysical Research: Solid Earth*, 114(B2),  
1431     2009.
- 1432 [79] Amir Sagy, Emily E Brodsky, and Gary J Axen. Evolution of fault-surface  
1433     roughness with slip. *Geology*, 35(3):283–286, 2007.
- 1434 [80] Francois Saucier, Eugene Humphreys, and Ray Weldon. Stress near geo-  
1435     metrically complex strike-slip faults: application to the san andreas fault  
1436     at cajon pass, southern california. *Journal of Geophysical Research: Solid*  
1437     *Earth*, 97(B4):5081–5094, 1992.

- 1438 [81] Heather M Savage and Michele L Cooke. Unlocking the effects of friction on  
1439 fault damage zones. *Journal of Structural Geology*, 32(11):1732–1741, 2010.
- 1440 [82] Jean Schmittbuhl, Sylvie Gentier, and Stéphane Roux. Field measurements  
1441 of the roughness of fault surfaces. *Geophysical Research Letters*, 20(8):639–  
1442 641, 1993.
- 1443 [83] Jean Schmittbuhl, Francois Schmitt, and Christopher Scholz. Scaling in-  
1444 variance of crack surfaces. *Journal of Geophysical Research: Solid Earth*,  
1445 100(B4):5953–5973, 1995.
- 1446 [84] Jean Schmittbuhl, Jean-Pierre Vilotte, and Stéphane Roux. Reliability of  
1447 self-affine measurements. *Physical Review E*, 51(1):131, 1995.
- 1448 [85] CH Scholz and JT Engelder. The role of asperity indentation and ploughing  
1449 in rock friction—i: Asperity creep and stick-slip. In *International Journal of*  
1450 *Rock Mechanics and Mining Sciences & Geomechanics Abstracts*, volume 13,  
1451 pages 149–154. Elsevier, 1976.
- 1452 [86] Ch H Scholz and CA Aviles. The fractal geometry of faults and faulting.  
1453 *Earthquake source mechanics*, pages 147–155, 1986.
- 1454 [87] Christopher H Scholz. Wear and gouge formation in brittle faulting. *Geology*,  
1455 15(6):493–495, 1987.
- 1456 [88] Richard A Schultz and Haakon Fossen. Displacement-length scaling in three  
1457 dimensions: the importance of aspect ratio and application to deformation  
1458 bands. *Journal of Structural Geology*, 24(9):1389–1411, 2002.

- 1459 [89] Paul Segall and DD Pollard. Mechanics of discontinuous faults. *Journal of*  
1460 *Geophysical Research: Solid Earth*, 85(B8):4337–4350, 1980.
- 1461 [90] Katherine AH Shervais and James D Kirkpatrick. Smoothing and re-  
1462 roughening processes: The geometric evolution of a single fault zone. *Journal*  
1463 *of Structural Geology*, 91:130–143, 2016.
- 1464 [91] Zheqiang Shi and Steven M Day. Rupture dynamics and ground motion from  
1465 3-d rough-fault simulations. *Journal of Geophysical Research: Solid Earth*,  
1466 118(3):1122–1141, 2013.
- 1467 [92] ZK Shipton and PA Cowie. Damage zone and slip-surface evolution over  $\mu\text{m}$   
1468 to km scales in high-porosity navajo sandstone, utah. *Journal of Structural*  
1469 *Geology*, 23(12):1825–1844, 2001.
- 1470 [93] Zoe K Shipton and Patience A Cowie. A conceptual model for the origin of  
1471 fault damage zone structures in high-porosity sandstone. *Journal of Struc-*  
1472 *tural Geology*, 25(3):333–344, 2003.
- 1473 [94] Zoe K Shipton, James P Evans, Kim R Robeson, Craig B Forster, and  
1474 Stephen Snelgrove. Structural heterogeneity and permeability in faulted  
1475 eolian sandstone: Implications for subsurface modeling of faults. *AAPG*  
1476 *bulletin*, 86(5):863–883, 2002.
- 1477 [95] Zoe K Shipton, Aisling M Soden, James D Kirkpatrick, Aileen M Bright,  
1478 and Rebecca J Lunn. How thick is a fault? fault displacement-thickness  
1479 scaling revisited. *Earthquakes: Radiated energy and the physics of faulting*,  
1480 pages 193–198, 2006.

- 1481 [96] RH Sibson. Fault rocks and fault mechanisms. *Journal of the Geological*  
1482 *Society*, 133(3):191–213, 1977.
- 1483 [97] Richard H Sibson. Crustal stress, faulting and fluid flow. *Geological Society,*  
1484 *London, Special Publications*, 78(1):69–84, 1994.
- 1485 [98] Mark W Stirling, Steven G Wesnousky, and Kunihiko Shimazaki. Fault  
1486 trace complexity, cumulative slip, and the shape of the magnitude-frequency  
1487 distribution for strike-slip faults: a global survey. *Geophysical Journal In-*  
1488 *ternational*, 124(3):833–868, 1996.
- 1489 [99] R Summers and J Byerlee. A note on the effect of fault gouge composition on  
1490 the stability of frictional sliding. In *International Journal of Rock Mechanics*  
1491 and *Mining Sciences & Geomechanics Abstracts*, volume 14, pages 155–160.  
1492 Elsevier, 1977.
- 1493 [100] Mark T Swanson. Sidewall ripouts in strike-slip faults. *Journal of Structural*  
1494 *Geology*, 11(8):933–948, 1989.
- 1495 [101] Anita Torabi and Haakon Fossen. Spatial variation of microstructure and  
1496 petrophysical properties along deformation bands in reservoir sandstones.  
1497 *AAPG bulletin*, 93(7):919–938, 2009.
- 1498 [102] Peter Vrolijk, Rod Myers, Michael L Sweet, Zoe K Shipton, Ben Dock-  
1499 rill, James P Evans, Jason Heath, and Anthony P Williams. Anatomy of  
1500 reservoir-scale normal faults in central utah: Stratigraphic controls and im-  
1501 plications for fault zone evolution and fluid flow. *Field Guides*, 6:261–282,  
1502 2005.

- 1503 [103] Weibin Wang and Christopher H Scholz. Wear processes during frictional  
1504 sliding of rock: a theoretical and experimental study. *JOURNAL OF GEO-*  
1505 *PHYSICAL RESEARCH-ALL SERIES-*, 99:6789–6789, 1994.
- 1506 [104] Naoto YOSHIOKA. Fracture energy and the variation of gouge and surface  
1507 roughness during frictional sliding of rocks. *Journal of Physics of the Earth*,  
1508 34(4):335–355, 1986.
- 1509 [105] O Zielke, M Galis, and PM Mai. Fault roughness and strength heterogene-  
1510 ity control earthquake size and stress drop. *Geophysical Research Letters*,  
1511 44(2):777–783, 2017.
- 1512 [106] Olaf Zielke and Paul Martin Mai. Sub-patch roughness in earthquake rupture  
1513 investigations. *Geophysical Research Letters*, 2016.

## 1514 **8 Appendix**

### 1515 **8.1 Surface Processing scripts**

1516 Or possibly a link to a git repository...

### 1517 **8.2 User manual for script**

1518 This manual should serve as both a basic guide to the logic and usage of the *surface*  
1519 *processing package*.

1520 The master function of the package is *surfaceprocessing*. This function effec-  
1521 tively deal with the inputs and direct computations towards the necessary func-  
1522 tions. Outputs of the function are a .mat workspace file for each input data file.

1523 The workspace includes a structure (called *parameters*) with the raw surface anal-  
1524 ysis outputs, the point spacing, the decimation factor (if any), the file name and  
1525 the date of the analysis. The workspace also includes the grid form of the origi-  
1526 nal inputed surface (called *surface*), and the pre-processed copy that was used for  
1527 the subsequent analysis (called *zGrid*). Inputs are always included in pairs. The  
1528 former defines the type of input, the latter qualifies or quantifies the input. This  
1529 structure allows for adaptability of the code to various needs. Options include the  
1530 following:

1531 • *what to do?*: 'toDo', followed by the desired analyses on of: 'FFT', 'PLOMB',  
1532 'parameters' or 'all' (default is 'all') - can be a cell array. This specifies what  
1533 kind of spatial analysis will be done on the input surface data. The spatial  
1534 analysis is calculated and averaged across every single profiles along the  
1535 surface. The analyses are the following:

1536 – 'FFT', a power spectrum computed using a Fast Fourier Transform  
1537 (FFT) algorithm;  
1538 – 'PLOMB', a power spectrum computed using a least-squares Lomb-  
1539 Scargle algorithm;  
1540 – 'paramters', the calculation (as a function of scale) of the Root Mean  
1541 Squared (RMS), skewness, kurtosis and asymmetry averaged across all  
1542 segments of a given length on all profiles of the surface.

1543 'all' simply performs all the analyses outlined above.

1544 • *skip pre-processing?*: 'bypass', followed by 'zygo', 'pre-processing' or 'no' to  
1545 be used input is already in aligned clean grid form - input files are then

1546 (default is 'no'). 'zygo' is specifically adapted to the proprietary data format  
1547 of the white light in Wong. 'pre-processing' simply skips any pre-processing.  
1548 This option requires a .mat structure with a field named 'grid' with the  
1549 topography and a field name 'pointSpacing' specifying the point spacing (in  
1550 meters). In either case the topography must be aligned such that the positive  
1551 x direction is the parallel direction.

1552 • *for the parameter analysis, how many scales?* 'numberOfScales' followed  
1553 by the desired number of analysed scales. This option is relevant to the  
1554 parameters analysis. Note that this has a lot of effect on the amount of  
1555 processing time (default is 10).

1556 • *decimation:* 'decimationFactor' followed by the desired decimation factor  
1557 (default is 1). Decimation is a useful tool to reduce computation time. The  
1558 surface grid is sub-sampled according to the decimation such that a decima-  
1559 tion factor of  $k$  would imply that only every  $k$ th point on the every  $k$ th will  
1560 be considered for hte subsequent analysis.

1561 • *Instrument specific analysis* 'instrument' followed by 'white light', 'laser  
1562 scanner' or 'lidar' (default does not set any instrument specific adjustments).  
1563 Some instrument specific pre-processing steps are taken. Please contact me  
1564 if you intend to use this as they may be highly dependent on the specific  
1565 instrument used.

1566 For instance, *surfaceprocessing('todo','FFT','bypass','zygo')* will only perform  
1567 a power spectral density analysis and will skip preprocessing and assume that all  
1568 input will be in the 'zygo' export .xyz format.

1569 When the command is executed, the user will be prompted to navigate to the  
1570 directory where the input data is located. IMPORTANT: the directory must *only*  
1571 contain files of one data format. There cannot be other files or sub-directories  
1572 in the directory. The user will then be prompted to choose a destination for the  
1573 output data. The requirements for the output location are less stringent. However,  
1574 it is advisable to choose an empty directory such as to facilitate subsequent steps.

1575 The next step is to visualize the output of the analysis. This is done using the  
1576 *unpack parameters* function. This function provides various visualization options  
1577 for all files in the directory chosen by the user. The first input (the *desired plot*)  
1578 can be one of the following:

1579       'FFT': plot all power spectra;

1580       'PLOMB': periodogram plot as determined by the Lomb-Scargle least squares  
1581 analysis;

1582       'topostd': plot of the root mean squared (RMS) as a function of scale;

1583       'topoSkew': plot of skewness of height fields as a function of segment scale;

1584       'topoKurt': plot of the the kurtoisis of height fields as a function of segment  
1585 scale;

1586       'PowerVsDisp': plot of power interpolated at a given scale as a function of  
1587 displacement;

1588       'RMSVsDisp': model RMS at a given scale as a function of displacement

1589       'Grids': shows both the original and pre-processed grid for the specified file  
1590       'fileName';

1591        '*Best Fits*': best logarithmic fits to power spectra obtained from the fast  
1592        fourrier transform analysis.

1593        The functionality of the packages is broadly divided into three sections: 1)  
1594        importing and preprocessing data, 2) performing various spatial statistics on the  
1595        pre-processed data, and 3) unpacking the analysis output into figures.

1596        In order to run smoothly the all functions included in the package should be  
1597        kept in the same directory or on an accessible path.

1598        For reference, here is a quick outline of what each function does:

1599        *affine fit*: (from mathworks) Computes the plane of best fit using least  
1600        squares normal distance;

1601        *align grid*: finds the smoothest directions in a grid using FFT spectra and  
1602        rotates and re-grids the input grid;

1603        *fault spectral density simple*: Calculates the average lomb-scargle spectral  
1604        density every row of a N by M array;

1605        *FindErr loop anisotropy*

1606        *flatten XYZ*: removes planar trends from XYZ data by applying a rotations  
1607        matrix according to the best fit plane (*affine fit*);

1608        *fractal model outlier*: Removes outlying segments according to a near-gaussian  
1609        model for the distribution of RMS values at specified segment lengths (or  
1610        scales);

1611        *frequency spectrum*: Calculates the average lomb-scargle spectral density of  
1612        all continuous segments on every single row of a N by M array;

1613        *parse 'zygo' format*: extracts the both the point spacing and topographic grid  
1614        from the exported zygo format. Can also remove planar trend from data  
1615        (substracted from grid);

1616        *rotateZ*: applies rotation matrix on XYZ data

1617        *surface 'analysis'*: Aggregates the analysis functions and applies them to an  
1618        input grid

1619        *surface 'cleaning'*: removes outliers associated with surface defects

1620        *surface 'parameters'*: calculates spatial statistics and parameters along seg-  
1621        ments as a function of scale (RMS, skewness, directional asymmetry and  
1622        kurtosis)

1623        *surface 'preprocessing' 2*: deals with preprocessing input data (import data,  
1624        cleaning and gridding data)

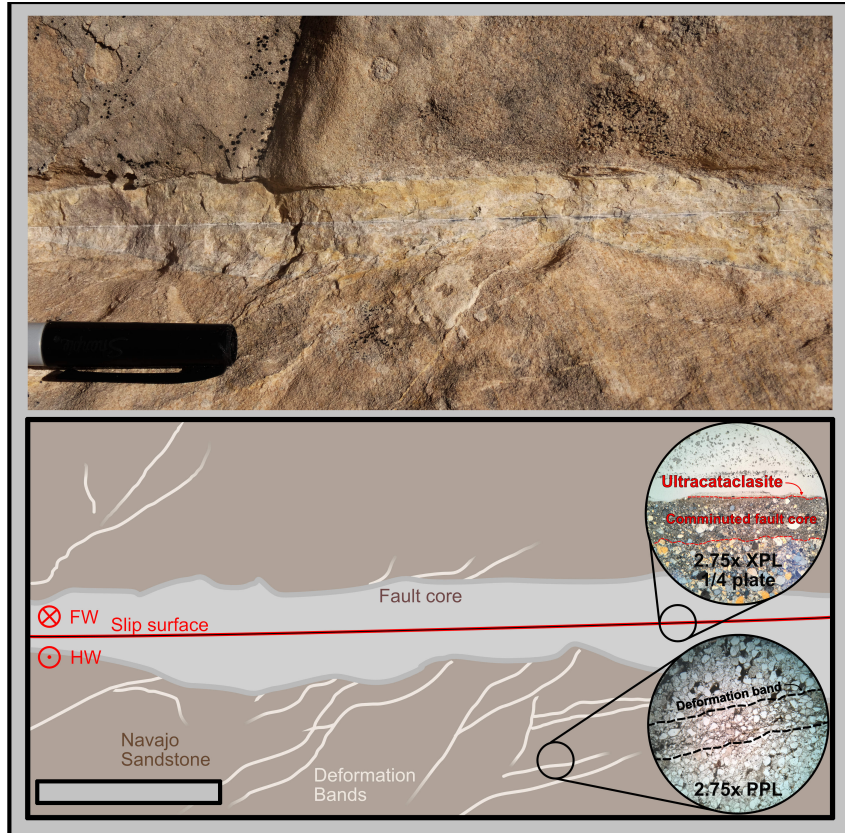


Figure 4: Top: Example of representative meso-structure of faults in the Navajo sandstone. Bottom: Cartoon of the representative meso-structure with slip surface (red), fault core (grey), deformation bands (pale beige) and intact host sand stone (brown). Upper half is the footwall; lower half is the hanging wall. Exposure is slip perpendicular. Representative thin sections show (not in situ) show the bottom half of the fault core (top) and deformation band (bottom). The section through the slip surface shows the microstructural architecture of slip surfaces with a very fine layer (barely visible) of ultracataclasite and a bounding comminuted layer. Note that this section is still well within the fault core. The section through the deformation bands shows the gradational reduction in grain size (outlined by black dashed line).

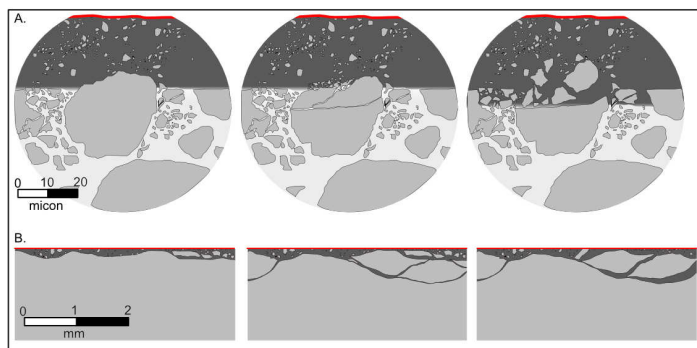


Figure 5: Schematic example of the interface between the cataclastic host and the fluidized ultracataclasite layer at two distinct length scales. A. at the length scale of ten's of microns grains, the shape of the interface is



Figure 6: Example of a slip surface interpreted as a principle slip surface with around 20 meters of displacement at Big Hole Fault



Figure 7: Left: Example of at least two distinct polished slip surfaces on the same fault structure. Right: Example of concentric pattern on cross-sectional view a fault

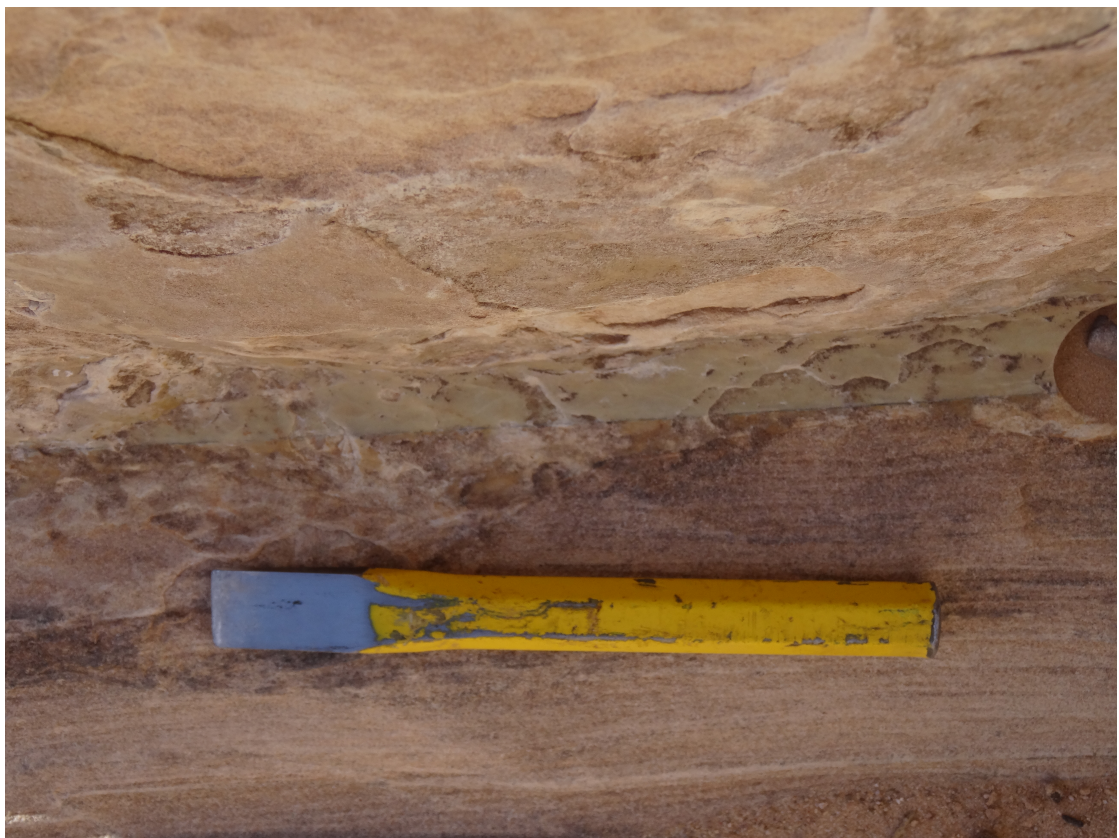


Figure 8: Example of a slip surface interpreted as a principle slip surface with around 20 meters of displacement at Big Hole Fault

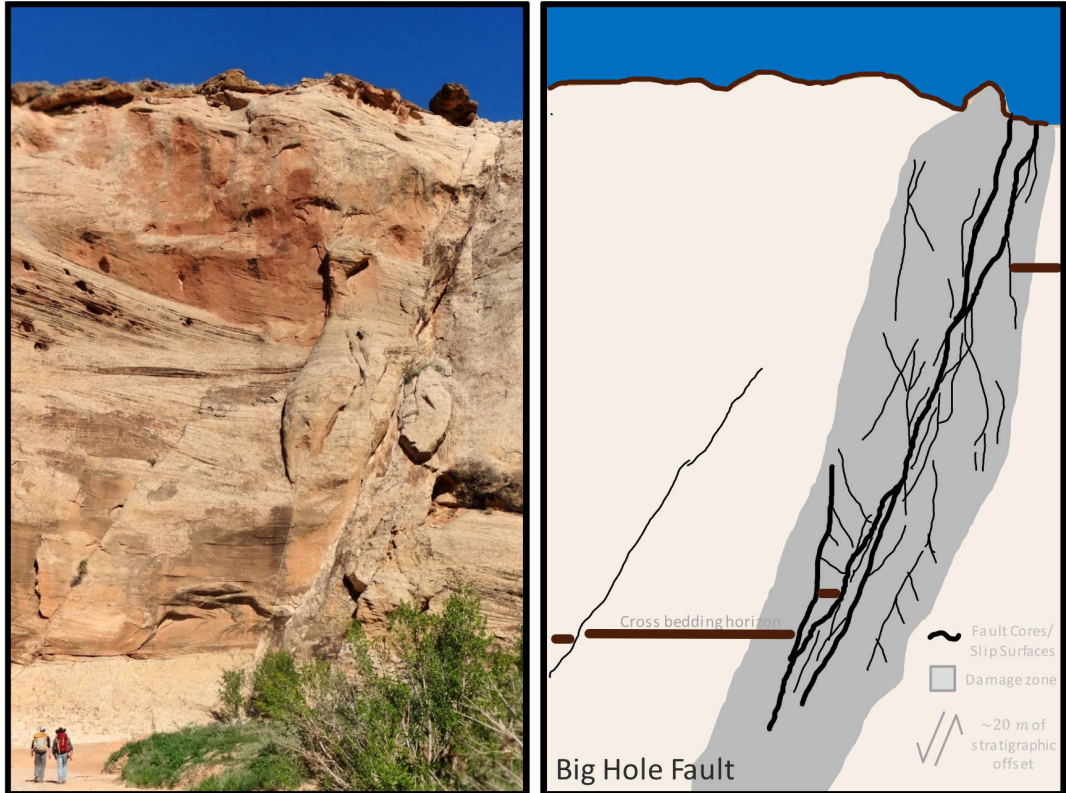


Figure 9: At Big Hole fault, two large-scale continuous strands of the fault, both accommodating meters of displacement exemplify problem at a larger scale. Due to the ambiguity, Shipton and Cowie, 2003 report large uncertainty on the partitioning of stratigraphic offset across the two strand